

**BULETINUL
INSTITUTULUI
POLITEHNIC
DIN IAȘI**

**Volumul 62 (66)
Numărul 3**

**Secția
MATEMATICĂ
MECANICĂ TEORETICĂ
FIZICĂ**

2016

Editura POLITEHNIUM

BULETINUL INSTITUTULUI POLITEHNIC DIN IAȘI
PUBLISHED BY
“GHEORGHE ASACHI” TECHNICAL UNIVERSITY OF IAȘI
Editorial Office: Bd. D. Mangeron 63, 700050, Iași, ROMANIA
Tel. 40-232-278683; Fax: 40-232-237666; e-mail: polytech@mail.tuiasi.ro

Editorial Board

President: **Dan Cașcaval**,
Rector of the “Gheorghe Asachi” Technical University of Iași
Editor-in-Chief: **Maria Carmen Loghin**,
Vice-Rector of the “Gheorghe Asachi” Technical University of Iași
Honorary Editors of the Bulletin: **Alfred Braier**,
Mihail Voicu, Corresponding Member of the Romanian Academy,
Carmen Teodosiu

**Editors in Chief of the MATHEMATICS. THEORETICAL MECHANICS.
PHYSICS Section**

**Maricel Agop, Narcisa Apreutesei-Dumitriu,
Daniel Condurache**

Honorary Editors: **Cătălin Gabriel Dumitraș**

Associated Editor: **Petru Edward Nica**

Scientific Board

Sergiu Aizicovici , University “Ohio”, U.S.A.	Liviu Leontie , “Al. I. Cuza” University, Iași
Constantin Băcuță , University “Delaware”, Newark, Delaware, U.S.A.	Rodica Luca-Tudorache , “Gheorghe Asachi” Technical University of Iași
Masud Caichian , University of Helsinki, Finland	Radu Miron , “Al. I. Cuza” University of Iași
Adrian Cordunenu , “Gheorghe Asachi” Technical University of Iași	Iuliana Oprea , Colorado State University, U.S.A
Constantin Corduneanu , University of Texas, Arlington, USA.	Viorel-Puiu Păun , University “Politehnica” of București
Piergiulio Corsini , University of Udine, Italy	Lucia Pletea , “Gheorghe Asachi” Technical University of Iași
Sever Dragomir , University “Victoria”, of Melbourne, Australia	Irina Radinschi , “Gheorghe Asachi” Technical University of Iași
Constantin Fetecău , “Gheorghe Asachi” Technical University of Iași	Themistocles Rassias , University of Athens, Greece
Cristi Foça , University of Lille, France	Behzad Djafari Rouhani , University of Texas at El Paso, USA
Tasawar Hayat , University “Quaid-i-Azam” of Islamabad, Pakistan	Cristina Stan , University “Politehnica” of București
Radu Ibănescu , “Gheorghe Asachi” Technical University of Iași	Wenchang Tan , University “Peking” Beijing, China
Bogdan Kazmierczak , Inst. of Fundamental Research, Warsaw, Poland	Petre P. Teodorescu , University of București
	Anca Tureanu , University of Helsinki, Finland
	Vitaly Volpert , CNRS, University “Claude Bernard”, Lyon, France

Secția

MATEMATICĂ. MECANICĂ TEORETICĂ. FIZICĂ

S U M A R

	<u>Pag.</u>
ANDREEA CELIA BENCHEA, DANIELA BĂBUȘCĂ și DANA ORTANSA DOROHOI, Energii de interacțiune în soluții a unor compuși de azobenzen (engl., rez. rom.)	9
OCTAVIAN BALTAG și MIUȚĂ RĂU, Magnetometru SQUID pentru detectarea semnalelor biomagnetice (engl., rez. rom.)	21
DANIELA IONESCU și GABRIELA APREOTESEI, Optimizarea densității de stocare pe suprafață în modul perpendicular folosind capuri de înregistrare particulare cu valvă de spin (engl., rez. rom.)	27
BOGDAN NEAGU și EUGEN NEAGU, Caracterizarea impedanței electrodului pentru stimulare profundă în creier: Spectroscopie de impedanță electrochimică în curent alternativ (engl., rez. rom.)	37
ELENA VASILICA GAFTON, GEORGIANA BULAI, IOAN DUMITRU, FLORIN TUDORACHE, OVIDIU F. CĂLȚUN, ADRIAN IULIAN BORHAN, ALEXANDRA RALUCA IORDAN și MIRCEA NICOLAE PALAMARU, Influența agenților de combustie și a tratamentelor termice asupra proprietăților oxizilor ferici de mangan (engl., rez. rom.)	51
ION SIMACIU, ZOLTAN BORSOS, ANCA BACIU și GEORGETA NAN, Orizontul accelerării și termodinamica particulei izolate (engl., rez. rom.)	65
IRINEL CASIAN BOTEZ, Procese nediferențiabile (engl., rez. rom.)	77

Section

MATHEMATICS. THEORETICAL MECHANICS. PHYSICS

CONTENTS		Pp.
ANDREEA CELIA BENCHEA, DANIELA BĂBUȘCĂ and DANA ORTANSA DOROHOI, Interaction Energies in Solutions of Azobenzene Compounds (English, Romanian summary)	9	
OCTAVIAN BALTAG and MIUȚĂ RĂU, SQUID Magnetometer for Biomagnetic Signal Detection (English, Romanian summary)	21	
DANIELA IONESCU and GABRIELA APREOTESEI, Areal Density Optimization at Perpendicular Recording Using Particular Spin Valve Heads (English, Romanian summary)	27	
BOGDAN NEAGU and EUGEN NEAGU, Impedance Characterization of a Deep Brain Stimulating Electrode: AC Electrochemical Impedance Spectroscopy (English, Romanian summary)	37	
ELENA VASILICA GAFTON, GEORGIANA BULAI, IOAN DUMITRU, FLORIN TUDORACHE, OVIDIU F. CĂLȚUN, ADRIAN IULIAN BORHAN, ALEXANDRA RALUCA IORDAN and MIRCEA NICOLAE PALAMARU, Influence of Combustion Agents and Thermal Treatment on Properties of Iron Manganese Oxides (English, Romanian summary)	51	
ION SIMACIU, ZOLTAN BORSOS, ANCA BACIU and GEORGETA NAN, The Acceleration Horizon and the Thermodynamics of Isolated Particle (English, Romanian summary)	65	
IRINEL CASIAN BOTEZ, Non-Differentiable Processes (English, Romanian summary)	77	

BULETINUL INSTITUTULUI POLITEHNIC DIN IAȘI
Publicat de
Universitatea Tehnică „Gheorghe Asachi” din Iași
Volumul 62 (66), Numărul 3, 2016
Secția
MATEMATICĂ. MECANICĂ TEORETICĂ. FIZICĂ

INTERACTION ENERGIES IN SOLUTIONS OF AZOBENZENE COMPOUNDS

BY

ANDREEA CELIA BENCHEA*, DANIELA BĂBUȘCĂ and
DANA ORTANSA DOROHOI

“Alexandru Ioan Cuza” University of Iași,
Faculty of Physics

Received: September 1, 2016

Accepted for publication: October 27, 2016

Abstract. The interaction energies between the components of dipolar solutions can be estimated on the bases of solvatochromic correlations which allow separating different types of interactions by their supply at the spectral shifts of the electronic absorption bands, spectral shifts induced by the modifications of the solvent nature. In the theory of the simple liquids, the dependence of the spectral shifts on the macroscopic parameters of the solvents allows to estimate some microscopic parameters of the spectrally active molecules.

Keywords: azobenzene compounds; interaction energies; theory of simple liquids; macroscopic/microscopic parameters.

1. Introduction

As a consequence of π -delocalization, aryl azo compounds have vivid colors, especially red, orange and yellow. Therefore, they are used as dyes, and are commonly known as azo dyes. Azo compounds are extensively utilized in chemical industries as dyes and pigments because of their extraordinary

*Corresponding author; *e-mail*: bencheacelia@yahoo.com

coloring (Khanmohammadi *et al.*, 2013; Kinali-Demirci, 2013). Moreover, in biological systems, some of these compounds could be used as inhibitors for tumor-growth (Ross and Warwick, 1955). Some important food colorants (*e.g.* sunset yellow and allura red) also belong to the class of azo dyes. Azo dyes contain the azo functionality, $-N=N-$, with attached aryl groups.

Solvents play an important role in physical and chemical processes. Additionally, solvent effect on absorption spectra can be used to provide information about solute–solvent interactions (Reichardt, 2005). Solute–solvent interactions are determined by the electronic and nuclear solvent polarization and they can be described by functions of the refractive index n and the electric permittivity ε :

$$f(n) = \frac{n^2 - 1}{n^2 + 1} \quad (1)$$

$$f(\varepsilon) = \frac{\varepsilon - 1}{\varepsilon + 2} \quad (2)$$

When the excited state of an azo dye is more polar than its ground state, the dye exhibits positive solvatochromism with a bathochromic (red) shift in the UV–Vis spectrum reflecting stabilization of the excited state in the polar solvent environment. Hypsochromic or blue shifts reflect stabilization of more non-polar excited states in more non-polar surroundings (Karukstis *et al.*, 2010).

Azobenzene compounds usually exhibit a low intensity $n-\pi^*$ absorption band in the visible range of the spectrum and a high intensity $\pi-\pi^*$ band in the UV spectra due to the conjugation between azobenzene and aromatic ring system (Airinei *et al.*, 2001).

2. Experimental Part

The azoderivatives (AZ1, AZ2) obtained in our laboratory was used upon purification by recrystallization. The solvents used were of spectrophotometric grade and supply by Aldrich or Fluka.

HyperChem 8.0.6 (www.hyper.com) is a molecular modelling program frequently utilized to determine some physical and structural parameters of different kinds of substances. To obtain a configuration characterized by a minimum free energy the molecules were geometrically optimized using the Polak Ribiere algorithm with maximum gradient set at $0.001 \text{ kcal}/(\text{mol} \cdot \text{\AA})$, after that through a single point calculation a number of physical and structural properties have been obtained. The Parametric Method number 3 is a semi-empirical method for the quantum calculation of molecular structure. PM3 (Stewart, 1989) uses the Hamiltonian and it is parameterized to reproduce a large number of molecular properties.

The electronic absorption spectra were recorded at a Specord UV Vis Carl Zeiss Jena Spectrophotometer with data acquisition system.

3. Results and Discussions

The optimized structures of some azo derivatives using the HyperChem 8.0.6. program are represented in Fig. 1 a) 4-aminoazobenzene (AZ1) and b) 4-acetamidoazobenzene (AZ2).

The studied molecules belong to the CS class symmetry: the molecules of this group are planar and they have only one element of symmetry, the plane of the molecules.

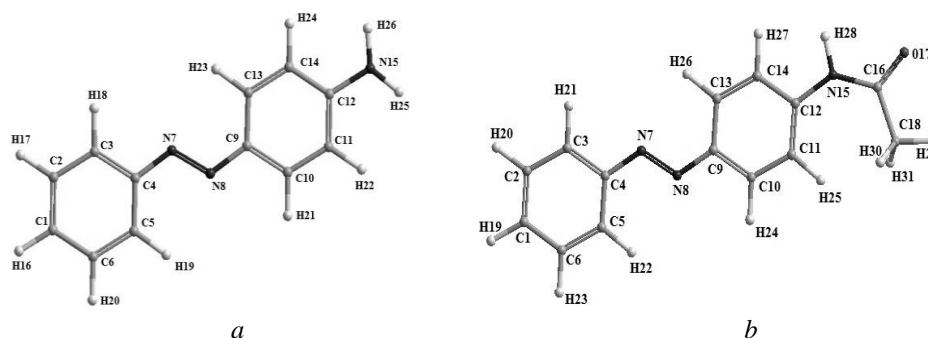
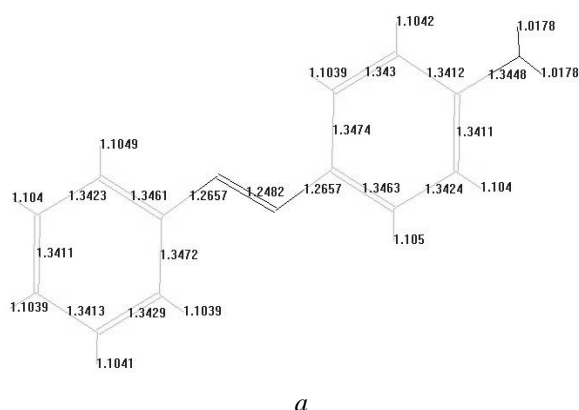
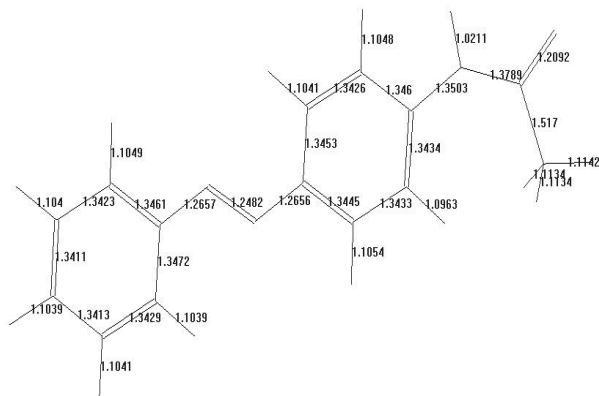


Fig. 1 – The optimized structures of AZ1 and AZ2 and the denomination of the atoms: a) AZ1; b) AZ2.

The bond lengths in [\AA] were computed for a) AZ1 and b) AZ2 are listed in Fig. 2.

The positions of the atoms are those from Fig. 1. The single bond C(12)-N(15) are longer than the single bonds C(4)-N(7) and C(9)-N(8) and also than the double bond N(7)-N(8), as it results from Fig. 2 a) AZ1.



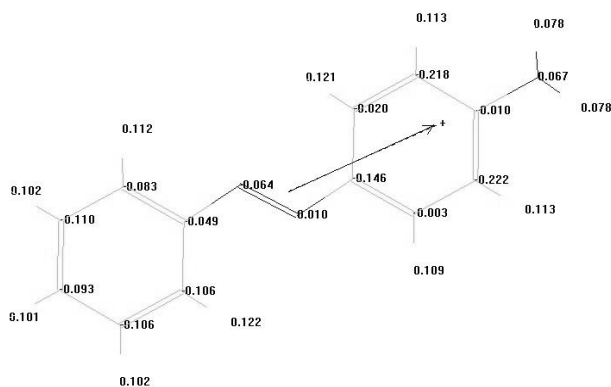


b

Fig. 2 – *a*) The computed bond lengths of AZ1 in [Å]; *b*) The computed bond lengths of AZ2 in [Å].

It is seen from Fig. 2 *b*) AZ2 that the single bonds N(15)-C(12) and N(15)-C(16) are smaller than the single bond C(16)-C(18) and also the double bonds N(7)-N(8) and C(16)-O(17) are smaller than the single bonds N(7)-C(4) and N(8)-C(9). In both Figs. *a*) and *b*) in benzene cycle the values of bond lengths are higher than 1.3 [Å].

The electronic charges on located near the molecular atoms in percents of electron elemental charge [$e = 1.6021662 \times 10^{-19}$ C] are given in Fig. 3 *a*) AZ1 and *b*) AZ2.



a

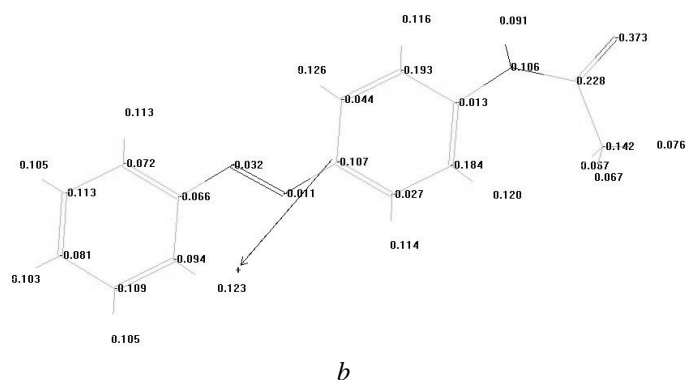


Fig. 3 – *a*) The atomic charges and the dipole moment orientation of AZ1 computed by HyperChem; *b*) The atomic charges and the dipole moment orientation of AZ2.

As one can see from Fig. 3 *a*) AZ1 that the negative charges are located near C, N atoms (the negative values are between -0.003 in C(10) atom and -0.032 in C(9) atom), and the positive charges are located near H atoms and also located near N(8) atom.

The negative charges are located near C, N and O atoms (the negative values are between -0.011 in N(8) atom and -0.372 in O(17) atom), and the positive charges are located near H atoms and also located near N(15) and C(16) atoms, as it results from Fig. 3 *b*) AZ2.

The Frontier Molecular Orbitals determine the molecular chemical stability, chemical reactivity and chemical hardness–softness of molecules, and playing an important role in the optical and electric properties (Fleming, 1976). It is also used to determine the interaction of the molecules with the other species. The energy levels of the molecular orbitals border HOMO (Highest Occupied Molecular Orbital) and LUMO (Lowest Unoccupied Molecular Orbital) for azo derivatives give information on the possible electronic transition.

They are highlighted in Fig. 4 AZ1 and Fig. 5 AZ2 (color: gray is positive value and black is negative value).

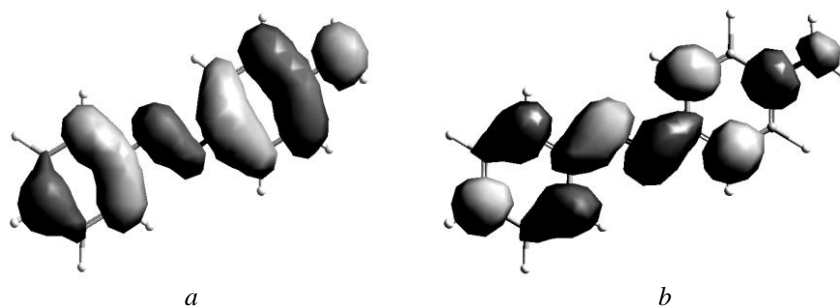


Fig. 4 – The frontier orbitals of 4-aminoazobenzene:
a) HOMO; *b*) LUMO.

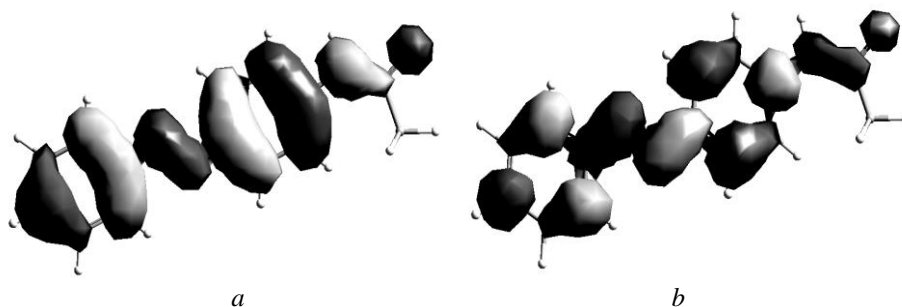


Fig. 5 – The frontier orbitals of 4-acetamidoazobenzene:
a) HOMO; b) LUMO.

The electrophilic attack occurs most likely to the atomic site with a high density of orbital HOMO while nucleophilic attack site is correlated with atomic high-density of orbital LUMO.

Table 1

The Energies Values in the Ground State for the Studied Molecules

Propertiers	AZ1	AZ2
Total energy, [kcal/mol]	-47788.527	-60742.463
Heat of formation, [kcal/mol]	175.626	132.851
Binding energy, [kcal/mol]	-2787.176	-2787.176
Electronic energy, [kcal/mol]	-292280.676	-389698.942
Nuclear energy, [kcal/mol]	244492.149	328956.478
E_{HOMO} , [eV]	-7.977	-8.492
E_{LUMO} , [eV]	-1.029	-1.458
$\Delta E = E_{\text{HOMO}} - E_{\text{LUMO}} $, [eV]	-6.948	-7.035

The AZ2 is more stable than the AZ1 due the higher negative value of the total energy (Table 1).

The difference $\Delta E = E_{\text{HOMO}} - E_{\text{LUMO}}$, known as HOMO/LUMO gap, represents the lowest energy electronic excitation that is possible in a molecule. For AZ1 this value is smaller than for molecule AZ2 and this demonstrate that molecule AZ2 is more available to interact with other species.

The ionization potential (I) and electron affinity (A) can be estimated from the HOMO and LUMO energy values by applying Koopmans theorem (Koopmans, 1934):

$$I = -E_{\text{HOMO}} \quad (3)$$

$$A = -E_{\text{LUMO}} \quad (4)$$

The density of the total electronic charge (Fig. 6), indicate areas with high or low electronegativity which determine the orientation of molecules.

Three regions with density of negative charge corresponding preferential coupling cation sites were highlighted for the studied molecules.

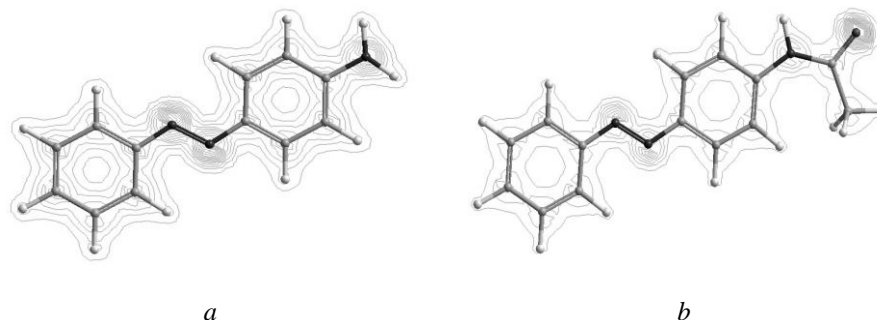


Fig. 6 – The density of the total electronic charge of the studied molecules:
a) AZ1; b) AZ2.

The dipole moment, the polarizability, the refractivity and logP were calculated using the QSAR method. Quantitative Structure - Activity Relationships (QSAR) correlate the molecular structure or properties derived from molecular structure with a particular chemical or biochemical activity (Gallegos, 2004).

Table 2
QSAR Parameters Calculated by HyperChem

Parameters	AZ1	AZ2
Surface area, [\AA^2]	401.43	457.97
Volume, [\AA^3]	625.46	731.90
Mass, [u.a.m]	197.24	239.28
Hydration energy, [kcal/mol]	-12.94	-9.87
Log P	0.25	0.08
Refractivity, [\AA^2]	75.55	82.99
Dipole moment, [D]	3.27	2.22
Polarizability, [\AA^3]	23.50	27.26

The hydration energy is defined as the energy absorbed when the substance is dissolved in water. The AZ1 have a higher values of the hydration energy than the AZ2. LogP represents the octanol/water partition coefficient, the positive values of logP shows that the studied compounds is lipophilic. The lipophilicity is a major determining factor in a compound's absorption and distribution in the body (Parthasarathi *et al.*, 2012). A more lipophilic compound will have low aqueous solubility, compromising bioavailability.

The Kamlet - Taft solvent parameters (Taft *et al.*, 1985) and Reichardt's parameters (Reichardt, 2005) used in LSER, the wavenumbers of electronic

absorption spectra, the polarizability function $f(n)$ and the polarity function $f(\varepsilon)$ are given in Table 3.

Table 3
UV-Vis Absorption Maxima and the Solvent Parameters for AZ1 and AZ2

No.	Solvent	$f(\varepsilon)$	$f(n)$	α	β	$\nu_{\text{exp.}} [\text{cm}^{-1}]$	
						AZ1	AZ2
1	n-Hexane	0.229	0.229	0	0	27660	28990
2	Cyclohexane	0.254	0.257	0	0	27510	28900
3	CCl4	0.292	0.273	0	0	27210	28610
4	Toluene	0.315	0.292	0	0.11	26670	28330
5	Chloroform	0.212	0.267	0.2	0.1	26880	28610
6	DCM	0.729	0.258	0.13	0.1	26700	28600
7	DCE	0.758	0.266	0	0	26600	28450
8	1-Pentanol	0.825	0.248	0.7	0.92	25910	28450
9	1-Butanol	0.849	0.237	0.84	0.84	25770	28560
10	2-Butanone	0.854	0.230	0.06	0.48	25640	28170
11	Acetone	0.870	0.220	0.08	0.48	25810	28250
12	Ethanol	0.890	0.221	0.86	0.75	25840	28570
13	Methanol	0.914	0.203	0.98	0.66	25910	28860
14	DMF	0.925	0.259	0	0.69	25030	27860
15	DM Acetamide	0.924	0.263	0	0.76	24720	27890
16	DMSO	0.939	0.282	0	0.76	24750	27780

Solvatochromic studies offer information about the strenght of the dispersive interactions by the spectral shifts measured in non-polar solutions.

The electronic absorbtion band of 4-aminoazobenzene (AZ1) and 4-acetamidoazobenzene (AZ2) in solvents having different physicochemical parameters has been recorded and the wavenumber in its maximum is listed in Table 3.

The equation which give the wavenumbers in the maximum of the band is:

$$\nu_{\text{calc.}} = \nu_0 + C_1 f(\varepsilon) + C_2 f(n) + C_3 \beta + C_4 \alpha \quad (5)$$

A multilinear dependence of the type Eq. (5) was used to describe the spectral shifts of two azobenzene derivatives measured in the solvents from Table 4.

Table 4
Characteristics of Eq. for Binary Solutions of Two Azobenzene Derivatives

Molecule	$\tilde{\nu}_0, [\text{cm}^{-1}]$	C_1	C_2	C_3	C_4	R
AZ1	29054.677	-1468.633	-5371.207	803.794	-1805.136	0.9233
AZ2	30160.118	-512.885	-5041.258	671.349	-682.334	0.9081

A good correlation was obtained as one can see in Table 4.

The calculated wavenumber in the maximum of the UV-Vis of 4-aminoazobenzene and 4-acetamidoazobenzene using equation mentioned above are plotted versus the corresponding experimental values in Fig. 9 a) AZ1 and b) AZ2.

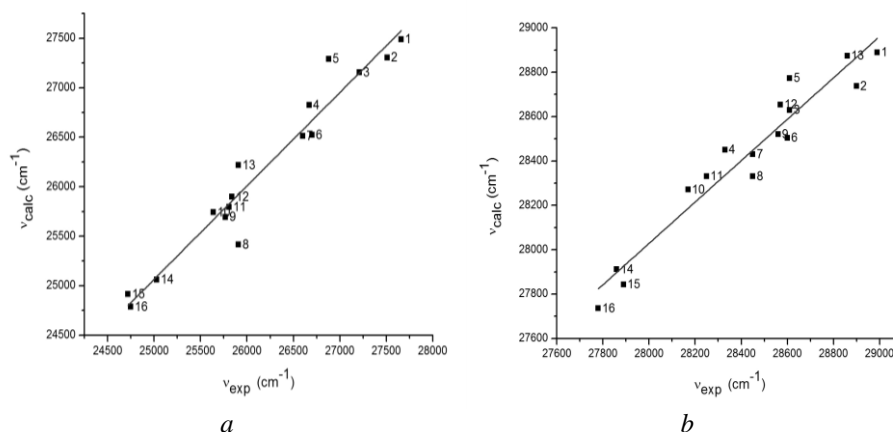


Fig. 9 – $\nu_{calc.}$ [cm^{-1}] versus $\nu_{exp.}$ [cm^{-1}]: a) AZ1; b) AZ2.

There is a good linear correlation between the calculated and experimental values of the wavenumbers in the maximum of the visible band of 4-aminoazobenzene Fig. 9a ($R = 0.94$, $SD = 218.13$) and for 4-acetamidoazobenzene Fig. 9b ($R = 0.93$, $SD = 94.70$).

4. Conclusions

Different solvents with different electric permittivities, refractive indices and Kamlet–Taft and Reichardt constants were used in this study, for to characterize the intermolecular interactions in binary solutions of two azobenzene derivatives.

The separation of the supply of the universal and specific interactions was made based on the correlation coefficients from the equations describing the solvatochromic effect (Rusu *et al.*, 2008).

Dispersive forces are predominant in non-polar solvents containing spectrally active molecules (Gheorghies *et al.*, 2008).

A series of azobenzene derivatives in the ground electronic state were analyzed from quantum-mechanical point of view and their electro-optical parameters were computed, and it demonstrate that the study compounds are lipophilic.

The results of this study could be used when azo-benzene derivatives are precursors in various chemical reactions.

REFERENCES

- Airinei A., Rusu E., Dorohoi D.O., *Solvent Influence on the Electronic Absorption Spectra of Some Azoaromatic Compounds*, Spectrosc. Lett., **34**, 1, 65-74 (2001).
- Gallegos S.A., *Molecular Quantum Similarities in QSAR: Applications in Computer – Aided Molecular Design*, Ph.D. Thesis, University of Girona, 2004.
- Gheorghieș C., Gheorghieș L., Dorohoi D.O., *Solvent Influence on Some Complexes Realized by Hydrogen Bond*, Journal of Molecular Structure, **887**, 122-127 (2008).
- Fleming I., *Frontier Orbitals and Organic Chemical Reactions*, John Wiley and Sons, New York, 1976.
- Karukstis K.K., Litz J.P., Garber M.B., Angell L.M., Korir K.G., *A Spectral Approach to Determine Location and Orientation of Azo Dyes within Surfactant Aggregates*, Spectrochimica Acta Part A, **75**, 1354-1361 (2010).
- Khanmohammadi H., Rezaeian Kh., Amini M.M., Weng Ng.S., *Azo-Azomethine Dyes with N, O, S Donor Set of Atoms and their Ni(II) Complexes: Synthesis, Characterization and Spectral Properties*, Dyes Pigments, **98**, 3, 557 (2013).
- Kinali-Demirci S., Demirci S., Kurt M., *Synthesis, Structure Characterization and Antimicrobial Evaluation of 4-(Substituted Phenylazo)-3,5-Diacetamido-1H-Pyrazoles*, Spectrochim. Acta Part A, **106**, 12 (2013).
- Koopmans T., *Über die Zuordnung von Wellenfunktionen und Eigenwerten zu den Einzelnen Elektronen Eines Atoms*, Physica (Elsevier), **1**, 1-6, 104-113 (1934).
- Parthasarathi R., Subramanian V., Roy D.R., Chattaraj P.K., *Bioorganic & Medicinal Chemistry*, In *Advanced Methods and Applications in Chemoinformatics: Research Progress and New Applications*, E.A. Castro, A.K. Haghi (Eds.) 2012.
- Reichardt C., *Solvents and Solvent Effects in Organic Chemistry*, VCH, New York, 2005.
- Ross W.C.J., Warwick G.P., *Reduction of Cytotoxic Azo Compounds by Hydrazine and by the Xanthine Oxidase–Xanthine System*, Nature, **176**, 298 (1955).
- Rusu E., Dorohoi D.O., Airinei A., *Solvatochromic Effects in Absorption Spectra of Some Azobenzene Compounds*, J. Mol. Struct., **887**, 1, 1-3, 216-219 (2008).
- Stewart J.J.P., *Optimization of Parameters for Semi-Empirical Methods I-Method*, Computational Chemistry, **10**, 2, 209 (1989).
- Taft R.W., Abboud J.L.M., Kamlet M.J., Abraham M.H., *Linear Solvation Energy Relations*, Journal of Solution Chemistry, **14**, 3, 153-186 (1985).
- www.hyper.com (HyperChem, Molecular Visualisation and Simulation Program Package, Hypercube, Gainesville, FL, 32601).

ENERGII DE INTERACȚIUNE ÎN SOLUȚII A UNOR
COMPUȘI DE AZOBENZEN

(Rezumat)

Energiile de interacțiune dintre componentele dipolare ale unei soluții pot fi estimate în cadrul studiilor solvatocromice care permit separarea diverselor tipuri de interacțiuni prin aportul acestora la deplasările unor benzi electronice de absorbție, deplasări cauzate de modificarea naturii solvenților folosiți. În baza teoriei lichidelor simple, dependența deplasărilor spectrale de anumiți parametri macroscopici ai solvenților permit estimarea unor parametri microscopici din starea excitată a moleculelor spectral active.

BULETINUL INSTITUTULUI POLITEHNIC DIN IAȘI
Publicat de
Universitatea Tehnică „Gheorghe Asachi” din Iași
Volumul 62 (66), Numărul 3, 2016
Secția
MATEMATICĂ. MECANICĂ TEORETICĂ. FIZICĂ

SQUID MAGNETOMETER FOR BIOMAGNETIC SIGNAL DETECTION

BY

OCTAVIAN BALTAG and MIUȚĂ RĂU*

“Grigore T. Popa” University of Medicine and Pharmacy, Iași,
Department of Medical Bioengineering

Received: November 5, 2016

Accepted for publication: December 15, 2016

Abstract. The paper presents theoretical and experimental results regarding the use of a SQUID magnetometer in detecting the biomagnetic fields, generated by bioelectric activity of the tissues. The work describes a SQUID magnetometer configured as a gradiometer, with first and second order and the electromagnetic environment in which such measurements can be made. Depending on the biological source, biomagnetic signal can have the induction value up to 50 pT. Considering a disturbing magnetic field source located at a given distance from the biological source, the work analyses the signal to noise ratio for the first and second order gradiometer configuration. Theoretical modelling shows an increasing signal noise ratio for the second order gradient of the magnetic field toward the simple measurement of the magnetic field or the first order gradient of the magnetic field. The signal noise ratio is even greater when the gradient is of higher order and the distance between the biomagnetic source and magnetic disturbance, increases. The experimental results show the SQUID gradiometer structure achieved and the recording of a biomagnetic signal generated by the heart's electrical activity – magnetocardiography.

Keywords: biomagnetometry; gradiometry; SQUID; magnetocardiography; magnetic shielded room.

*Corresponding author; *e-mail*: miuta.carmina@gmail.com

1. Introduction

Biomagnetic field measurements is a very special subdomain in magnetometry and is confronted with some difficult aspects such as the very small value of the measured parameters, which is from 10^{-15} T (the smallest) for the field generated by foetal heart to 10^{-12} T (the highest) generated by the adult heart and a poor signal/noise ratio (SNR) for these type of measurements. The omnipresence of environmental electromagnetic fields, with much higher values than the biomagnetic fields determines a poor signal/noise ratio and the necessity to carry out the measurements in spaces where the environmental electromagnetic fields are diminished to smaller values or comparable with the measured parameters, in order to improve the SNR. When it speaks about magnetic fields, the SNR refers to the level of the biomagnetic fields against the level of environmental electromagnetic fields and natural noises specific to the utilized magnetic sensor. The environmental magnetic and electromagnetic field spectrum is complex; therefore the methods to mitigate it are sophisticated from a conceptual and constructive standpoint. With these aspects in mind, the researches were focused on the diminution of ambient noise and/or on the development of certain measuring devices less sensitive to electromagnetic and magnetic environment. These developed systems with very high sensitivity threshold known up to now, for very weak magnetic field measurement, very versatile, are Superconducting Quantum Interference Device or SQUID, which are flux-voltage converters; they can measure any physical parameter that can be converted in magnetic flux (magnetic field, magnetic field gradient, magnetic susceptibility, voltage, current, mechanical displacement). One of the mostly known methods to improve the SNR is to configure, physically a classical magnetometric structure in a gradiometric structure. The gradiometers are preferable mainly because of their ability to detect magnetic field gradients and reject common vector of magnetic field.

2. Theoretical Aspects and Description of Gradiometer

The gradiometric structure is composed of two coaxial coils, with the same number of turns and identical sections, located in parallel planes, at a fixed distance, named baseline, connected in opposition in flux transformer circuit. This is the 1st order gradiometer but can obtain gradiometers with higher order by combining a desired numbers of first order gradiometers.

The biogradiometer was configured from a SQUID biomagnetometer and has three SQUID coaxial coils. The magnetometer sensors are connected through flux transformers to three independent electronic modules, such that to obtain three magnetometric channels.

The adopted solution is advantageous due to the fact that, from the three SQUID magnetometer channels, one can realize several SQUID gradiometers by using the electronic subtraction of the signal arrived from the three individual magnetometric channels (Baltag and Rău, 2015). By electronic subtraction produced at the output of the three channels, a four channel gradiometer was realized using the electronic subtraction operation at the output of the three channels, namely: two 1st order gradiometers with baseline $\Delta z = 4$ cm, a 1st order gradiometer with baseline $\Delta z = 8$ cm and 2nd order gradiometer with baseline $\Delta z = 4$ cm. The configured gradiometer is shown in Fig. 1.

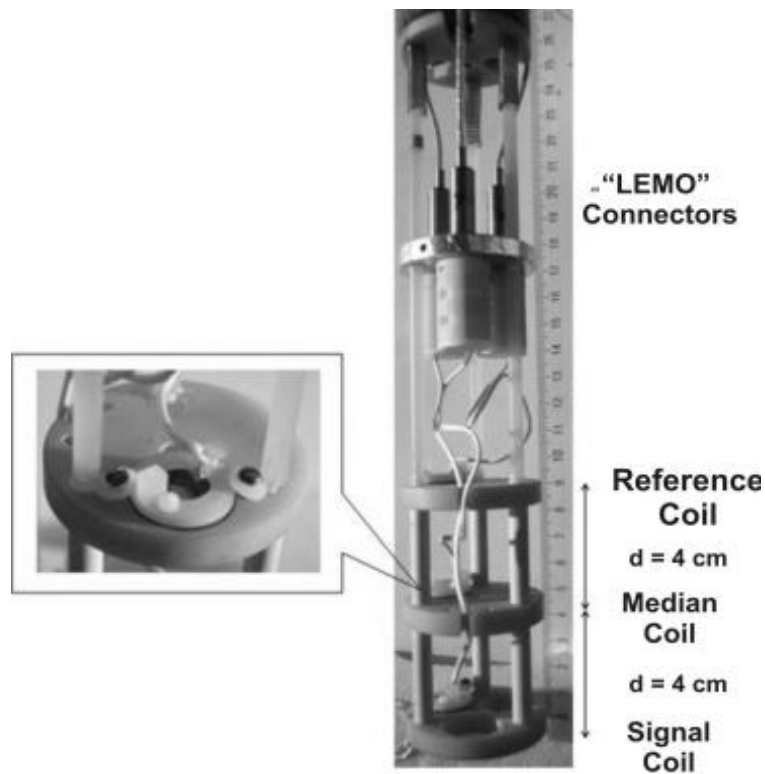


Fig. 1 – SQUID gradiometer.

For the operations of calibration and verification of the SQUID transducer, a Helmholtz coil was realized with a small field constant (comparable with biomagnetic fields); this permits to apply both fields and field gradients of known values.

Considering the magnetic moment of the biomagnetic source, M_s and the magnetic moment of the disturbance source M_p , one can compute, the SNR for the first order gradient, Eq. (1):

$$\left(\frac{S}{P}\right)_1 = \frac{G_s^1}{G_p^1} = \frac{M_s}{M_p} \frac{r_p^4}{r_s^4} \quad (1)$$

and for the second order gradient, one can compute the same ratio:

$$\left(\frac{S}{P}\right)_2 = \frac{G_s^2}{G_p^2} = \frac{M_s}{M_p} \frac{r_p^5}{r_s^5} \quad (2)$$

where S and P are signal respectively, perturbation (noise) source and r_p and r_s are the distance between the gradiometer SQUID and the perturbation source respectively biomagnetic source. Computing the ratio between the two relations it follows that the signal noise ratio is increased with a r_p/r_s factor, Eq. (3).

$$\frac{(S/P)_2}{(S/P)_1} = \frac{r_p}{r_s} \quad (3)$$

In practice, the factor $r_p/r_s < 100$.

We have analyzed the distribution with the distance of the magnetic field and of the 1st and 2nd order gradients produced by the two sources, one of disturbances and one of biosignal, and we found out that it is more advantageous to measure the 2nd order gradient than the 1st order gradient, as the SNR is improved, see Fig. 2 (Baltag and Rău, 2014).

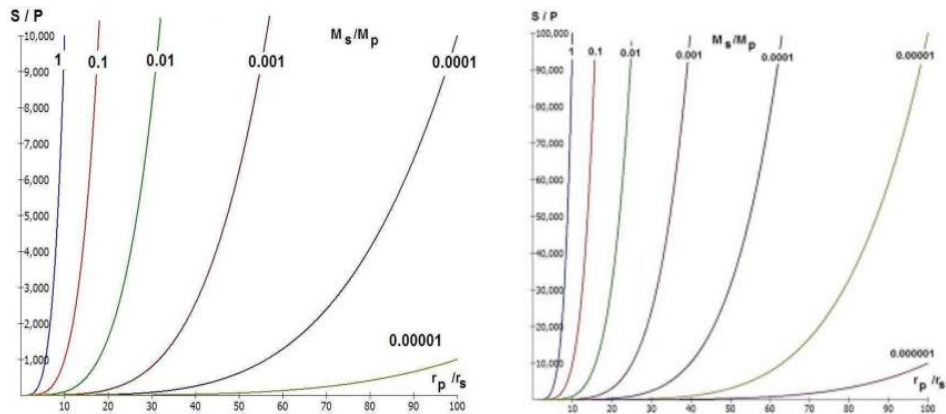


Fig. 2 – SNR for first and second order gradient.

3. Experimental Results

Given the fact that the SQUID magnetometer, an instrument with a very low sensitivity threshold, manifests some limitations connected with immunity from the external magnetic and electromagnetic environment, besides some precautions for providing an adequate screening, one must also take into account the electromagnetic conditions of the location. The configured SQUID biogradiometer is working properly only in a magnetic shielded rooms (RMS) sized (2x2x3)m with a dynamic system for annulment of the magnetic field, which is formed by a triaxial system of Helmholtz coils sized (4x4x4) m.

The squid gradiometer was used to record for the first time, in Romania, a biosignal generated by adult heart, a magnetocardiogram. The morphological aspects of the signal processed are very similar with the ECG signal, Fig. 3.

In the recorded magnetocardiogram signal one can establish the existence of some disturbing components produced by parasite external fields (50 Hz). The existence of the non-biological noise was also established in the absence of the examined patient. Therefore, an additional filtration of the obtained signal is necessary, being aware that it is mixed with this noise with the dominant frequency of 50 Hz in whose spectrum are also present the second and the third harmonics. In order to remove the residual signal of 50 Hz that appears at the gradiometer output, each electronic subtraction channel has in its composition circuits for phase correction of the residual signal of 50 Hz. The phase shifter permits the correction of 50 Hz residual phase such that to obtain a minimal residual signal at the output. Its peak to peak amplitude is of 21.6 pT_{pp}.

The obtained MCG signal is a primary signal. It was the first MCG signal recording in laboratory condition, from Romania (Rău, 2012).

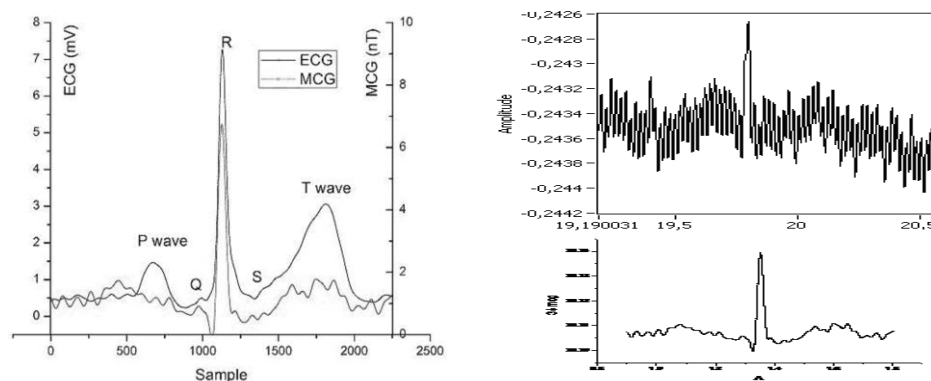


Fig. 3 – MCG/ECG signal.

4. Conclusions

The biogradiometer was configured from a SQUID biomagnetometer and has three SQUID coaxial coils. For theoretical aspects, we considering a disturbing magnetic field source located at a given distance from the biological source and analyses the SNR for the first and second order gradiometer configuration. Theoretical modelling shows an increasing SNR for the second order gradient of the magnetic field toward the simple measurement of the magnetic field or the first order gradient of the magnetic field. The SNR is even greater when the gradient is of higher order and the distance between the biomagnetic source and magnetic disturbance, increases. The morphological aspects of the obtained MCG biosignal are similar with the ECG biosignal.

REFERENCES

- Baltag O., Rău M.C., *SQUID Gradiometer for Biomagnetic Fields*, Advancements of Medicine and Health Care Through Technology, Cluj-Napoca, 2014.
- Baltag O., Rău M.C., *Factors Affecting the Performance of a SQUID Gradiometer*, The 9th International Symposium on Advanced Topics in Electrical Engineering, Bucharest, 2015.
- Rău M.C., *Researches in Biomagnetic Fields Measurements*, Ph.D. Thesis, “Gheorghe Asachi” Technical University of Iași, 2012.

MAGNETOMETRU SQUID PENTRU DETECTAREA SEMNALELOR BIOMAGNETICE

(Rezumat)

Lucrarea prezintă rezultatele teoretice și experimentale referitoare la o instalație biomagnetometrică realizată de autori. Rezultatele teoretice demonstrează faptul că măsurătorile biomagnetometrice realizate în regim de gradiometrie au un raport semnal/zgomot mai mare decât cele realizate în regim clasic, iar între cele două tipuri de gradiometre acest raport este mai mare pentru măsurătorile făcute cu gradiometrul de ordin doi decât pentru cele făcute cu gradiometrul de ordin unu. Rezultatele experimentale au condus la performanța înregistrării primului semnal magnetocardiografic în România.

BULETINUL INSTITUTULUI POLITEHNIC DIN IAȘI
Publicat de
Universitatea Tehnică „Gheorghe Asachi” din Iași
Volumul 62 (66), Numărul 3, 2016
Secția
MATEMATICĂ. MECANICĂ TEORETICĂ. FIZICĂ

AREAL DENSITY OPTIMIZATION AT PERPENDICULAR RECORDING USING PARTICULAR SPIN VALVE HEADS

BY

DANIELA IONESCU^{1,*} and GABRIELA APREOTESEI²

“Gheorghe Asachi” Technical University of Iași,

¹Department of Telecommunications

²Department of Physics

Received: November 6, 2016

Accepted for publication: December 14, 2016

Abstract. A category of metallic spin valves for read heads presenting colossal magnetoresistance changing have been analyzed by simulation methods, using the 3D HFSS program. Hard ferromagnetic alloys were considered in the stack of the nanometric magnetic/spacer/magnetic layers, based on Fe and Co and a proper spacer, working in the current-perpendicular-to-plane (CPP) mode. The magnetoresistance changes (MR , [%]) were calculated by theory and from simulation data, under different condition of exploitation, in function of the thickness of the hard magnetic layer and spacer, average grain size, and applied field respectively. Results indicate us monotone evolutions for some specific sub-domains and present maxima when the structure parameters can be correlated. A magnetoresistance ratio of about 0.4...2% have been computed, dependent on layers nature and thickness, for the alloy grain sizes up to 7-8 nm and an applied field of 2-10 kOe. Data were used for obtaining high resolution reading performances, which to overcome the reported results.

Keywords: magnetoresistance; spin valve; thin film; spin current; areal density.

*Corresponding author; *e-mail*: danaity@yahoo.com

1. Introduction

A category of metallic spin valves for read heads presenting colossal magnetoresistance changing have been analyzed by simulation methods, using the 3D HFSS program by Ansoft.

The read heads explore the bits traveling through the recording media (the disk surface). In the case of the perpendicular recording, the bits point up or down perpendicular to the disk surface, in comparison with the parallel recording case, where the bits are moving in the disk plane (Jogo *et al.*, 2007; Nagasaka *et al.*, 2006). Higher fields are necessary at perpendicular recording to set the magnetization, but the advantage is that the magnetization is more stable.

The ultrahigh-density recording with areal densities over hundreds of Gb/in², can be achieved by exploiting the properties of the tunnel magnetoresistive (TMR) heads (Tanaka *et al.*, 2002) implemented into the spin valves for read heads. A few structures of this type have been analyzed in this paper and their properties have been determined in order to correlate the parameters to optimize the structure.

2. Characterization of the Spin Valve Materials

Hard ferromagnetic metallic alloys have been considered in the spin valves, based on Fe and Co and a proper spacer, working in the current-perpendicular-to-plane (CPP) mode (Fig. 1).

The stack of layers was considered as follows (from top to bottom):

- a soft magnetic layer, on top of the stack - the free layer, with free oriented magnetization. Materials were chosen like Co₂MnSi, Co₂CuSn (Heusler alloys) or NiFeCo, with thicknesses of 5...10 nm.
- a spacer layer, of Cu alloy, + Pt (8%), Ni (14%), with thicknesses of 2...4 nm. This represents a non-magnetic spacer, with role of exchange decoupler between the magnetic layers.
- a reference layer, with the same nature like the soft layer: Heusler alloys or NiFeCo, with thicknesses of 12...25 nm
- a inter-layer, of Ru (a heavy metal), with thicknesses of 1...2 nm, the finer layer, where the most of the exchange interactions occurs
- a hard magnetic layer, which is the pinned layer, with fixed direction of the magnetization. The same Heusler alloys of NiFeCo were considered for this layer, with thicknesses of 20...30 nm. The layer is placed at the basis of the stack, on a substrate which maintains its magnetization direction.
- a substrate, represented by an oxide, MgO (001) or NiO. This is the pinning layer, antiferromagnetic, which fixes the bottom layer magnetization and raises its coercivity.

The current-perpendicular-to-plane (CPP) geometry was chosen, where the sensing current flows perpendicular to the layers.

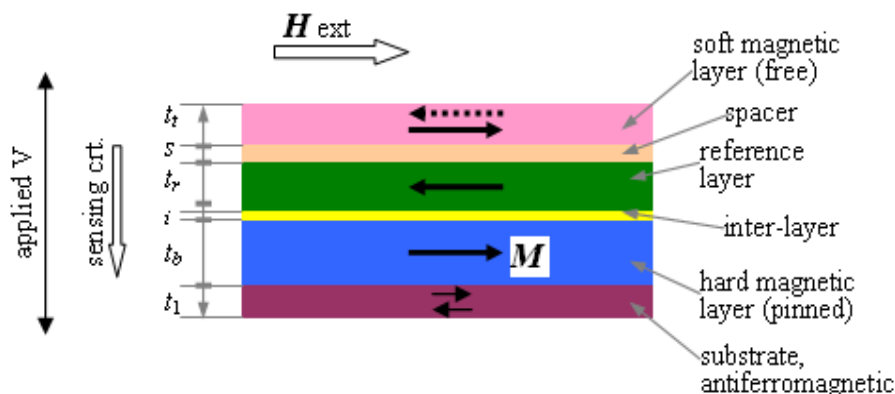


Fig. 1 – The considered layers configuration in the spin valve head. Sensing current flows perpendicular to the ferro / nonferro-magnetic interfaces, in the current-perpendicular-to-plane (CPP) geometry.

The spin valve working in this geometry presents a greater magnetoresistance ratio δ_H , which ensures a greater sensitivity to the device than in the case of the parallel geometry. The theoretical model was based on the Valet-Fert theory (Valet and Fert, 1993) - the theory for giant magnetoresistance (GMR) in the spin valves with CPP geometry. The current which is passed perpendicular to the ferro / nonferro-magnetic interfaces it is assumed that presents an uniform current density uniform across the area. The electronic transport in magnetic multilayers depends on the electrons scattering phenomena due to the spin-orbit interactions.

An important parameter considered at simulations was the spin-diffusion lengths l_{sf} , which represents the average distance over which the electrons diffuses between the spin-relaxation events and it is linked by the losses. These events are more rare in comparison with the electron scattering events which occurs at current passing through the stack of layers.

In a spin valve, the perpendicular magnetoresistance ratio can be computed with the formula (Bass, 2013):

$$\rho = \sum_{i=1}^n \left(\frac{1 - \cos \phi_i}{2} \right)_i \quad (1)$$

where $\Phi_i = \theta_{\text{bottom},i} - \theta_{\text{top},i}$ is the difference in the magnetization angle between a grain from the bottom hard magnetic layer and a grain in the adjacent reference layer, n = total number of grains. The presence of a percentage of structural defects was taken into account at simulation.

For estimating the MR of the considered spin valves using the simulation data, another formula has been applied, using the sensing current which transforms the change in resistance in a readback voltage (Hirota *et al.*, 2013; Sharma, 2009), given by simulation:

$$\frac{dR}{R} = \frac{R(H) - R(0)}{R(0)} \quad (2)$$

where $R(H)$ is the resistance of the sample in a magnetic field H , and $R(0)$ is the resistance in null field.

The specific resistance, AR represents the product of the area A through which an uniform CPP current flows and the sample resistance R . Variation of this parameter is $\Delta AR = AR_{anti} - AR_{\parallel}$, which represents the difference between the specific resistances in the anti-parallel and parallel states (magnetizations of adjacent ferromagnetic layers in the stack) (Hirota *et al.*, 2013; Rychkov *et al.*, 2009). On the context, the CPP magnetoresistance ratio was considered as:

$$MR_{CPP}[\%] = \frac{\Delta AR}{AR_{anti\parallel}} \quad (3)$$

3. Results for Magnetoresistance Changes

For the considered magnetic materials in the spin valve (Co_2MnSi , Co_2CuSn or NiFeCo), the magnetoresistance changes (MR , [%]) were calculated by theory and from simulation data, under different condition of exploitation.

Dependence of the MR , [%] on physical and geometrical parameters of the successions of nanometric magnetic/spacer/magnetic (anti-parallel magnetized) layers have been determined and represented on graphs. A sense current, I , of 0...3 mA has been considered in the stack.

Parametrical representations of the magnetoresistance ratio on thickness of the hard magnetic layer and spacer, average grain size, and applied field respectively, indicate us monotone evolutions for some specific sub-domains and present maxima which are of interest in practice. In order to obtain better results in material exploitation, we have focused on correlation of the parameters which ensure a maximal response of the structure (spin valve read head), on the basis of simulation results.

The CPP magnetoresistance ratio of the considered spin valves in function of the average grain size of the hard magnetic layer was given in Fig. 2.

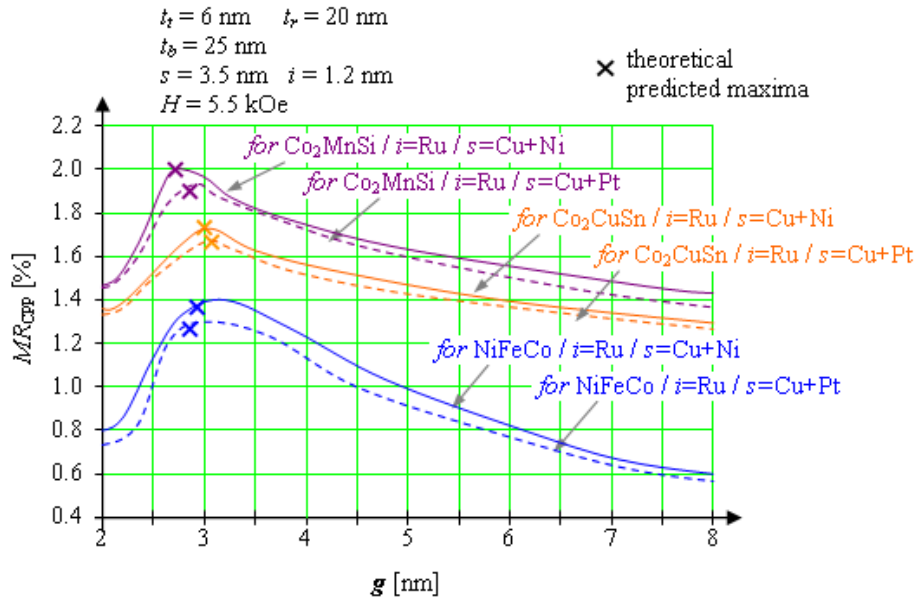


Fig. 2 – The CPP magnetoresistance ratio of the considered spin valves in function of the average grain size of the hard magnetic layer. Simulation and theoretical maxima were illustrated on graphs.

Simulations have indicated us that the interlayer exchange coupling field decreases when the hard layer thickness increases. Coupling depends on grain sizes, consequently smaller grains are equivalent with a higher magnetoresistance. MR dependence on g is resonant, the maximum occurring also at lower values for g in the hard magnetic material.

Theoretical predicted maxima are of lower magnitude and slightly shifted in respect with simulation maxima, due to the fact that the theoretical model do not take into account all the influences and parameters interdependence considered in the simulations, from the lattice level to grains, interfaces and thin film level.

The CPP magnetoresistance ratio for the considered magnetic materials in the spin valves in function of the applied magnetic field H was illustrated in Fig. 3. For clarity reason, we have focused on the curves corresponding to the higher magnitude of the maximum, when spacer / inter-layer thickness varies, which were illustrated on graphs for each material.

Change in magnetoresistance presents resonant evolutions in function of the field, the maximum which characterizes the interaction (magnetization - spins - field) being high and sharp. One can conclude that the device operation out of maximum area is not of interest in practice. The maximum position has to be determined and simulation offers a non-destructive reliable method.

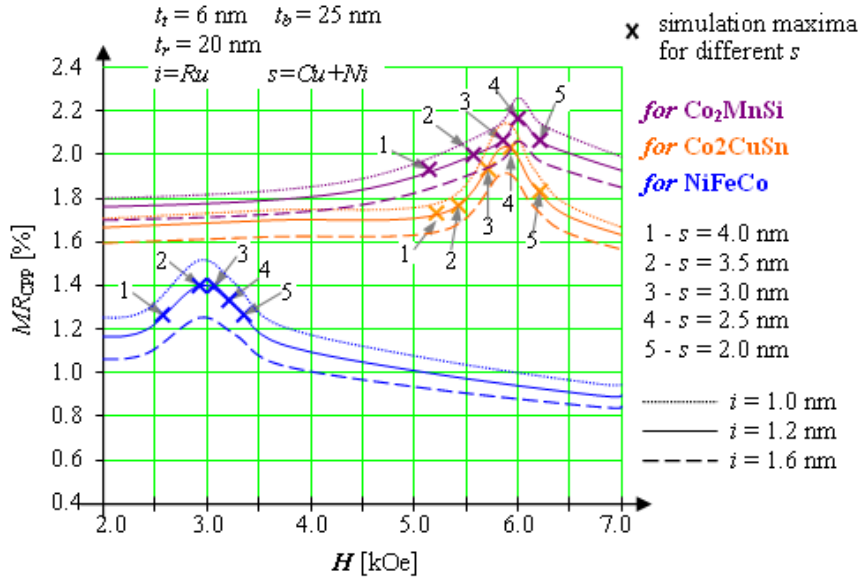


Fig. 3 – The CPP magnetoresistance ratio of the considered hard magnetic materials in the spin valves in function of the applied magnetic field H . Curves corresponding to the higher magnitude of the maximum, when spacer / inter-layer thickness varies, were illustrated on graphs for each material.

The simulations have also indicated that, for a given hard magnetic material, spacer nature imposes the magnitude report of the maxima for different curves.

The changes in the CPP magnetoresistance ratio in function of the spacer layer thickness s , for the considered combinations of materials in the spin valve, are given in Fig. 4. The MR ratio presents an increasing and then a decreasing with s , with a wide maximum, which is more wide and flat than magnetic material magnetization is lower. If the spacer thickness has greater values than the value corresponding to the MR ratio maximum, greater is the s , weaker the interlayer interactions and weaker the MR .

We have also to consider the presence of current shunting effects, when electrons preferentially flow through the thicker spacer instead of undergoing scattering at the magnetic layer/spacer interfaces. This determines in practice a slight decreasing of the MR ratio values, no more than a few percents.

Our studies, based on physical considerations (Bass, 2013; Eid *et al.*, 2002), use the simulational parametrical analysis for explaining the MR ratio maximum causes: the hysteresis phenomenon (maximum magnitude depends on the value of the hysteresis magnetization – field); the presence of defects, in particular of the Pinhole defects, which degrade significantly the MR due to the direct interactions between the magnetic layers.

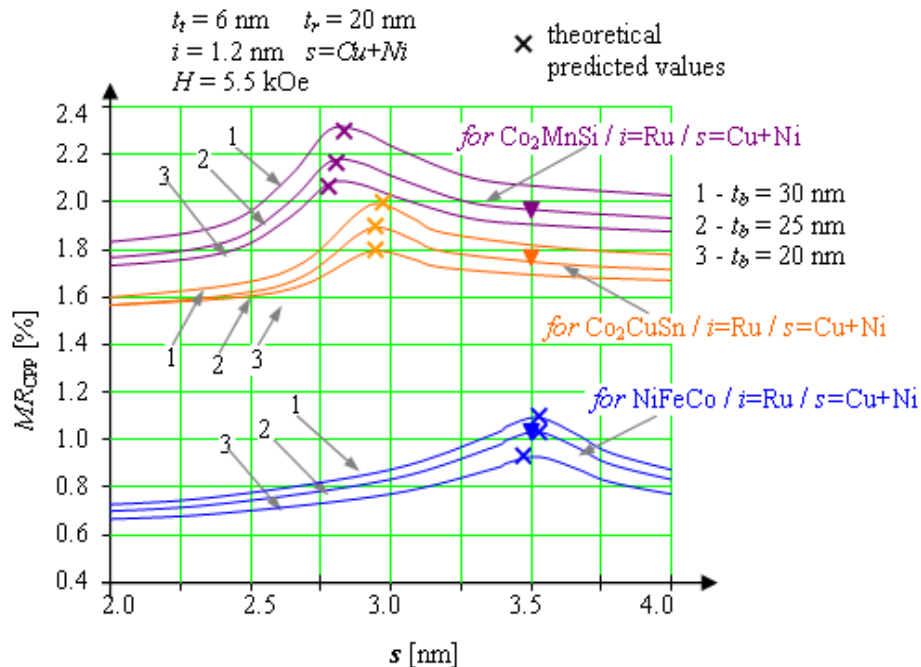


Fig. 4 – The CPP magnetoresistance ratio of the considered hard magnetic materials in the spin valves in function of the spacer layer thickness s , for the considered combinations of materials in the spin valve. Theoretical predicted maxima were indicated on graphs.

As a conclusion of our study, the areal density of hard disk drives in function of the CPP magnetoresistance ratio of the considered spin valves was represented in Fig. 5. The presence of groups of single and multiple maxima can be noticed on graphs.

The main structural maxima of the areal density are imposed by the magnetic ion in the hard magnetic alloy and their characteristics depend on the internal interactions in the exchange coupled system, hard - soft magnetic. A few interaction maxima, generally less intense, are controlled by other factors, like the resonant coupling phenomena between structure, external field and sensing current.

By modifying different parameters of the structure, maxima with magnitude depending on the spin current were identified. Their originate in the magnetization dynamics, which is determined by the torques moving the spins, torques generated by the exchange interaction between conduction electrons and DW magnetizations, under the influence of external magnetic field.

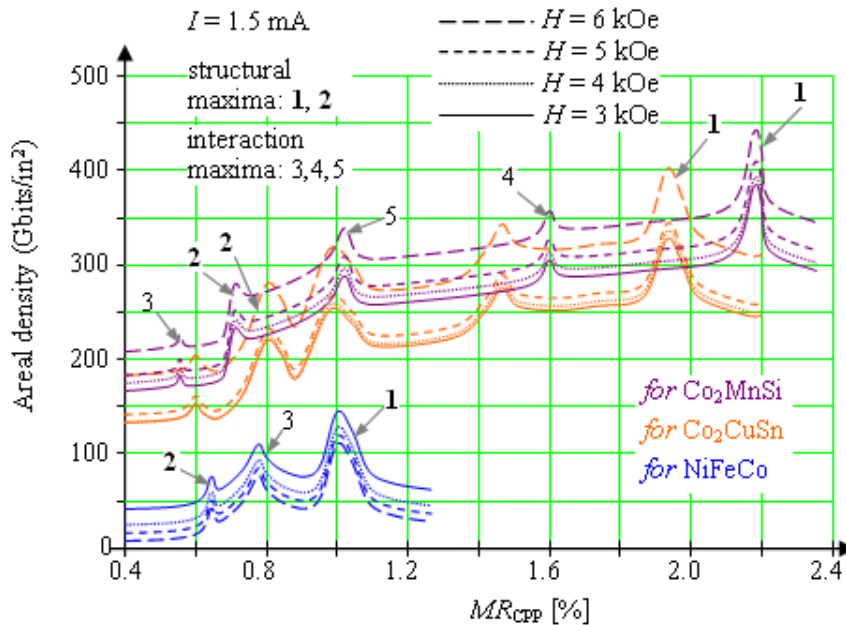


Fig. 5 – Areal density of hard disk drives in function of the CPP magnetoresistance ratio of the considered spin valves. Structural, respectively interaction maxima were illustrated on graph.

4. Structure Optimization and Conclusions

A set of new magnetic materials (& Heusler alloys) have been considered in this paper, placed in a nano-layered structure inside a spin valve for read heads. The advantages of such a kind of structures for specific applications were illustrated, when the structure parameters can be correlated using the results given by the 3D structural simulation.

For the considered spin valve structures we have computed a magnetoresistance ratio of about 0.4...2.2%, dependent on the magnetic/spacer layers nature and thickness, for alloy grain sizes up to 7-8 nm and an applied field of 2-10 kOe.

For ultrahigh-density recording, an areal density of a few hundred of Gb/in² was found, with maxima depending on the magnetoresistance changes at structure level. Our purpose was the parameter correlations in order to obtain maxima of the magnetoresistance ratio associated with a maximal areal density, for high resolution reading performances, which to overcome the results reported until now.

Our simulational data have been able to indicate solutions for a better response of the considered spin valves in the subdomains of parametrical

computed maxima. The set of parameters of interest can be extracted from graphs represented on the basis of simulation results and generates the structure implementation.

REFERENCES

- Bass J., *Current Perpendicular-to-Plane (CPP) Magnetoresistance (MR)*, Materials Science (cond-mat.mtrl-sci), arXiv:1305.3848, Mesoscale and Nanoscale Physics (cond-mat.mes-hall), 2013.
- Eid K., Fonck R., AlHaj Darwish M., Pratt Jr. W. P., Bass J., *Current-Perpendicular-to-Plane-Magnetoresistance Properties of Ru and Co/Ru Interfaces*, J. Appl. Phys., **91**, 8102 (2002).
- Hirota E., Sakakima H., Inomata K., *Giant Magneto-Resistance Devices*, Springer Science & Business Media, 2013.
- Jogo A., Nagasaka K., Ibusuki T., Shimizu Y., Tanaka A., Oshima H., *Current-Perpendicular Spin Valves with High-Resistivity Ferromagnetic Metals for Ultrahigh-Density Magnetic Recording*, J. of Magnetism and Magnetic Materials, **309**, 1, 80-86 (2007).
- Nagasaka K., Jogo A., Ibusuki T., Oshima H., Shimizu Y., Uzumaki T., *CPP-GMR Technology for Future High-Density Magnetic Recording*, Fujitsu Sci. Tech. J., **42**(1), 149-157 (2006).
- Rychkov V.S., Borlenghi S., Jaffres H., Fert A., Waintal X., *Spin Torque and Waviness in Magnetic Multilayers: A Bridge Between Valet-Fert Theory and Quantum Approaches*, Phys. Rev. Lett., **103**, 066602 (2009).
- Sharma A., *Spintronics with Metals: Current Perpendicular-to-the-Plane Magneto-Transport Studies*, Dissertation Thesis, Michigan State University, ProQuest LLC, UMI Number 3348217, 2009.
- Tanaka A., Shimizu Y., Seyama Y., Nagasaka K., Kondo R., Oshima H., Eguchi S., H. Kanai H., *Spin-Valve Heads in the Current-Perpendicular-to-Plane Mode for Ultrahigh-Density Recording*, IEEE Transactions on Magnetics, **38**, 1, 84-88 (2002).
- Valet T., Fert A., *Theory of the Perpendicular Magnetoresistance in Magnetic Multilayers*, Phys. Rev. B Condens Matter, **48**, 10, 7099-7113 (1993).

OPTIMIZAREA DENSITĂȚII DE STOCARE PE SUPRAFAȚĂ ÎN MODUL PERPENDICULAR FOLOSIND CAPURI DE ÎNREGISTRARE PARTICULARE CU VALVĂ DE SPIN

(Rezumat)

A fost analizată prin metode de simulare o categorie de valve de spin metalice prezentând magnetorezistență gigant, folosite pentru capuri de citire, cu ajutorul programului 3D HFSS. În stiva de straturi nanometrice magnetic/separator/magnetic au

fost considerate aliaje feromagnetice de înaltă rezistivitate pe bază de Fe, Co și Al, cu un material potrivit ca strat separator, funcționând în modul de operare curent-perpendicular-pe-plan (CPP). Modificările de magnetorezistență (ΔR) au fost calculate din considerente teoretice și în paralel cu ajutorul datelor obținute prin simulare, în diferite condiții de exploatare, funcție de grosimea stratului magnetic dur și a separatorului, de dimensiunea grăunților cristalini și respectiv de câmpul aplicat. Rezultatele ne indică evoluții monotone pentru unele subdomenii specifice și prezintă maxime când parametrii structurali pot fi corelați. A fost calculat un raport al magnetorezistenței (MR) de circa 0.4...1.7%, dependent de natura și grosimea straturilor, pentru dimensiuni ale grăunților cristalini ai aliajului de până la 7-8 nm și un câmp aplicat de 2-10 kOe. Datele au fost folosite pentru obținerea unei proces de citire performantă de înaltă rezoluție a datelor, cu rezultate superioare celor raportate până în prezent.

BULETINUL INSTITUTULUI POLITEHNIC DIN IAȘI
Publicat de
Universitatea Tehnică „Gheorghe Asachi” din Iași
Volumul 62 (66), Numărul 3, 2016
Secția
MATEMATICĂ. MECANICĂ TEORETICĂ. FIZICĂ

IMPEDANCE CHARACTERIZATION OF A DEEP BRAIN STIMULATING ELECTRODE: AC ELECTROCHEMICAL IMPEDANCE SPECTROSCOPY

BY

BOGDAN NEAGU¹ and EUGEN NEAGU^{2,3,*}

¹Toronto Western Research Institute, University Health Network and Division of Neurology,
Department of Medicine, University of Toronto, Toronto, Canada

²Universidade Nova de Lisboa, Caparica, Portugal,
Departamento de Ciência dos Materiais

³“Gheorghe Asachi” Technical University of Iași,
Department of Physics

Received: November 18, 2016

Accepted for publication: December 16, 2016

Abstract. The impedance of the Medtronic 3387 deep brain stimulation (DBS) electrode was characterized using electrochemical impedance spectroscopy (EIS). The interface meta-saline was modeled as a parallel combination of faradaic resistance ($R_F(f,j)$) and double layer capacitance ($C_{dl}(f,j)$). The model took in consideration the dependence of $R_F(f,j)$ and $C_{dl}(f,j)$ of frequency f and current density j . The coupling capacitance between the metallic wires was included in the model. $C_{dl}(f,j)$ and $R_F(f,j)$ were determined from the fit of the data to the electrical model. We documented a significant frequency-dependent voltage drop on the interface and it influences the spread of the stimulation voltage. The electrical efficiency of the electrode was small for low frequencies, increased to 56% at 3 kHz and was constant for higher frequencies.

Keywords: metal-saline interface; impedance spectroscopy; deep brain stimulation.

*Corresponding author; *e-mail*: euneagu1@yahoo.com

1. Introduction

The Medtronic 3387 DBS electrode (Medtronic® Inc, Minneapolis, MN, USA) is used in therapy (stimulation) or electrophysiological recordings. Constant voltage (voltage-controlled) stimulation imposes a voltage spread within the brain that depends on the impedances of the contact-electrolyte interface and of the tissue (Butson and McIntyre, 2005; Miocinovic *et al.*, 2009). The frequency and j dependence of the impedance of the contact-electrolyte interface can be monitored with EIS (Macdonald, 1992; Cogan, 2008). Few studies report on the interface impedance behavior for j above the linearity limit (Ragheb and Geddes, 1990; Schwan and Maczuk, 1965; Geddes *et al.*, 1971). The impedance was measured *in vitro* (Holsheimer *et al.*, 2000; Wei and Grill, 2009) or *in vivo* (Wei and Grill, 2009) using biphasic constant-voltage pulses (Holsheimer *et al.*, 2000), biphasic square current pulses and sinusoidal signals of 1 Hz to 10 kHz (Wei and Grill, 2009). EIS measurements were carried on a scaled-down version of the DBS electrode, suitable for implantation in the non-human primate brain (Lempka *et al.*, 2009).

A detailed description of the electrical impedance of the Medtronic 3387 DBS electrode and the contact-saline interface with stimulation settings relevant for therapy is currently lacking. This is because the design of the DBS electrode is complex from the electrical impedance measurements point of view. Also it has been difficult to determine the interface impedance from the measurements because the saline impedance (bulk impedance) was approximated with the asymptotic high frequency impedance (Holsheimer *et al.*, 2000; Wei and Grill, 2009). Overlooking the impedance of the contact-electrolyte interface can affect the volume of neuronal activation (McIntyre *et al.*, 2004), the tendency for tissue damage (McCreery *et al.*, 1990) and electrode corrosion (Shepherd and Clark, 1991).

Previous electrical models of the Medtronic 3387 DBS electrode neglected the coupling capacitance between the leads (Holsheimer *et al.*, 2000; Wei and Grill, 2009). An accurate description of the electrode impedance and of the contact-saline interface impedance will further our knowledge in several directions: understand the relation between the stimulation voltage and the current passing through tissue *in vivo*, establish a relation between the stimulation voltage and the voltage actually delivered to the tissue, analysis of the *in vivo* EIS data and for the development of computational models of neural recording and stimulation.

The goal of this study was to propose a quantitative electrical model for the DBS electrode impedance and the contact-saline interface. The model accounts for the nonlinear dependence of $R_F(f,j)$ and $C_{al}(f,j)$ with frequency and current density. Our results complete the previous published work on DBS electrode.

2. Methods

Broad-band EIS was performed for two adjacent contacts of the Medtronic 3387 DBS electrode (the electrode has four platinum iridium contacts, Fig. 1).

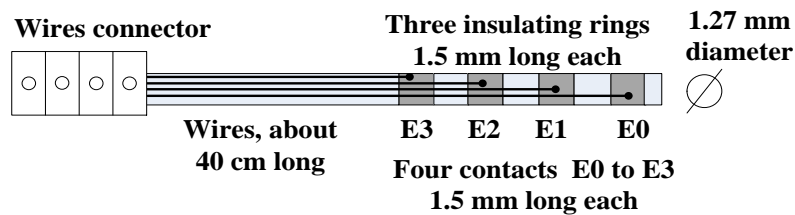


Fig. 1 – The Medtronic 3387 electrode for deep brain stimulation.

2.1. Electrochemical Impedance Spectroscopy

Sine wave signal was used to measure the impedance using a QuadTech 7600 Precision Resistance-Capacitance-Inductance meter. The range of stimulation frequencies was 10 Hz to 2 MHz with 106 frequency points, 20 points for a frequency decade, spaced logarithmically. We used constant current (0.3 to 6 mA rms; j from 5 to 100 mA cm⁻²) and voltage-controlled stimulation signals (0.3 to 1 V, rms). If not otherwise noted, the reported results are for 1 V rms voltage-controlled sinusoidal signal or for 1 mA rms constant current. These values are relevant for therapeutic stimulation settings. Measurements were performed in a tank filled with 2 l saline, placed in a Faraday cage. Measurements were carried in different saline concentrations for two reasons: i) the electrical conductivity of the tissue can be lower than that of 0.9% saline; ii) to detect the variation of $C_{dl}(f,j)$ and $R_f(f,j)$ with saline conductivity. At the same time an encapsulation layer may form on the surface of the electrode which is equivalent to a decrease of the electrical conductivity of the medium. Unless otherwise noted, the saline was 0.154 M NaCl (9 g/l, conductivity 1.5 S m⁻¹). In addition to measurements in saline, the impedance was measured: with the DBS electrode in the air to measure the coupling capacitance between the leads (C_{le}), including the individual contacts of the DBS electrode, and the electrical resistance (R_l) of the 2x40 cm long leads; with the DBS electrode in distilled water to estimate the capacitance between two adjacent contacts (C_{cl}). If not otherwise noted, the measurements were replicated three times at identical conditions and the mean values are presented.

2.2. Electrical Model of the DBS Electrode

2.2.1. Electrode in the Air

The impedance of the leads running from the DBS electrode connectors to the contacts, $Z_l(f)$, has real and imaginary components. The real component (R_l) is determined by the length of the metallic leads between the DBS electrode connectors and the contacts and by the resistance of the insulating material around the metallic leads R_d . The imaginary component of $Z_l(f)$ has three parts: (i) the coupling capacitance C_{le} between the metallic leads running from the DBS electrode connector to the contacts, (ii) the inductance of the leads which is small and was neglected and (iii) the capacitance C_{cl} between the two adjacent contacts. R_d is important during measurements with the electrode in the air. The equivalent circuit of the DBS electrode in the air is shown in Fig. 2a.

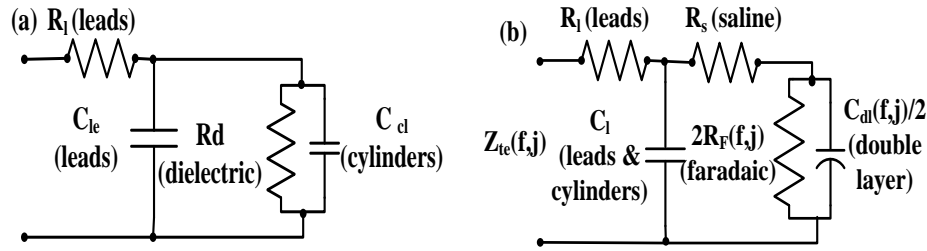


Fig. 2 – a) The equivalent circuits of the DBS electrode in air for the case of bipolar configuration; b) The equivalent circuits of the DBS electrode in saline solution for the case of bipolar configuration.

2.2.2. Electrode in Saline

We made the following assumptions: (i) R_d was negligible, thus C_{le} and C_{cl} appeared connected in parallel and they were replaced by C_l ; (ii) the two electrode–saline interfaces have the same impedance characteristics.

R_s was in series with the interface impedance $Z_{dl}(f,j)$ which consisted of an f and j dependent double layer capacitance $C_{dl}(f,j)/2$ in parallel with an f and j dependent faradaic resistance $2R_F(f,j)$. The equivalent circuit of the DBS electrode in saline is shown in Fig. 2b. The parallel equivalent circuit of the electrode consists of $R_p(f,j)$ in parallel with $C_p(f,j)$. The impedance of the DBS electrode measured in saline was $Z(f,j)$. The theoretical impedance (components showed in Fig. 2b) was $Z_{te}(f,j)$. To determine $C_{dl}(f,j)$ and $R_F(f,j)$ we need an analytical equation for $Z_{te}(f,j)$. We assumed that:

$$C_{dl}(f, j) = \frac{C_{dl0}(j)}{f^n} \quad (1)$$

and:

$$R_F(f, j) = \frac{R_{F0}(j)}{f^m} \quad (2)$$

where $C_{dl0}(j)$ (units Fs^{-n}) was a measure of the double layer capacitance at 1 Hz, n was a measure of the deviation from pure capacitive behavior, $R_{F0}(j)$ (units Ωs^{-m}) was a measure of the faradaic resistance at 1 Hz and m was a measure of the deviation from pure ohmic behavior.

3. Results

3.1. Resistance of the Lead Wires

With the electrode in the air and contacts E1 and E2 short-circuited, R_l was $86.4 \pm 0.3 \Omega$ (5 measurements), comparable with previous results (Holsheimer *et al.*, 2000; Wei and Grill, 2009).

3.2. Electrode Impedance

The measured $C_p(f)$ and $R_p(f)$ of the electrode in air, distilled water or saline (0.4, 2 and 9 g/l) are shown in Fig. 3 for 1V rms. Similar results were reported by measurements in buffered saline solution with frequencies in the range 1 Hz to 10 kHz (Wei and Grill, 2009).

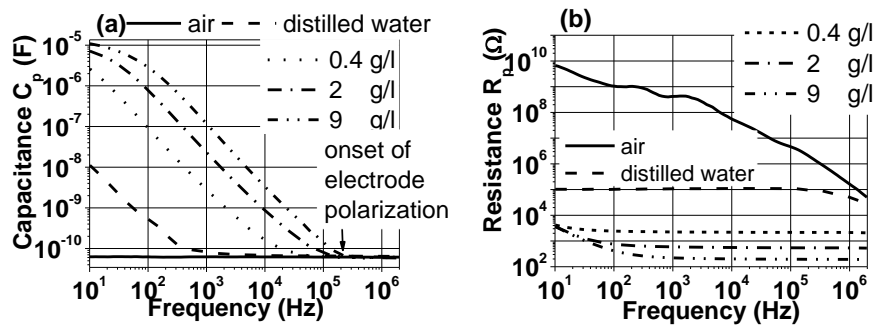


Fig. 3 – a) The equivalent parallel capacitance $C_p(f)$ of the DBS electrode. The arrow indicates the onset of electrode polarization. The onset frequency is lower as the saline concentration is lower; b) The equivalent parallel resistance $R_p(f)$ of the DBS electrode. Above a certain frequency which increases with saline concentration R_p is frequency-independent and allows to calculate the geometry factor.

Clinical measurements of the DBS electrode impedance reported values between 415 and 1999 Ω (Coffey, 2008). These values are higher than the

values reported in Fig. 3b for 0.9% NaCl concentration. Data in Fig. 3b allows to calculate the geometry factor (GF) as 0.0058 m for bipolar configuration and 0.0049 m for monopolar configuration. The electrode capacitance increased with decreasing frequency due to the ion charges accumulating at the metal-saline interface (Bard and Faulkner, 1980; Ackmann and Seitz, 1984; McAdams and Jossinet, 1995). The onset of electrode polarization was clearly observed (Fig. 4a) while complete electrode polarization (the frequencies for which the capacitance was constant) was not. The capacitance of the Medtronic DBS electrode was estimated to be 3.3 μF (Butson and McIntyre, 2005) or 1.5 μF (Holsheimer *et al.*, 2009). Our results showed that 3.3 μF was the capacitance at 112 Hz in 0.9% saline. The equivalent resistance $R_p(f)$ increased at low frequencies and the increase was higher for higher NaCl concentration. The capacitive or resistive nature of the current depends on the frequency and the conductivity of the solution. This is why we tested a large range of saline concentrations. The main contribution to $C_p(f)$ was given by the double layer capacitance, yet $C_p(f)$ does not represent the double layer capacitance. The double layer capacitance and the faradaic resistance will be obtained by fitting the data to the analytical model we presented.

3.3. Impedance Dependence on Current Density

Because the double layer impedance changes with j (Bard and Faulkner, 1980; Lempka *et al.*, 2009; Schwan, 1968), the electrode impedance changes with j . Fig. 4 shows the measured impedance $|Z_t(f,j)|$ and $C_p(f,j)$ with the DBS electrode in physiologic saline for 0.3, 1 and 6 mA. The impedance decreased when the current increased. The dependence of the impedance with j decreased when f increased. For frequencies higher than 3 kHz the impedance was independent of j . Fig. 4b showed that for low frequencies the capacitance increased with j . For frequencies higher than 300 Hz, the capacitance did not depend on j . For frequencies higher than 3 kHz, the resistance was independent of j (data not shown).

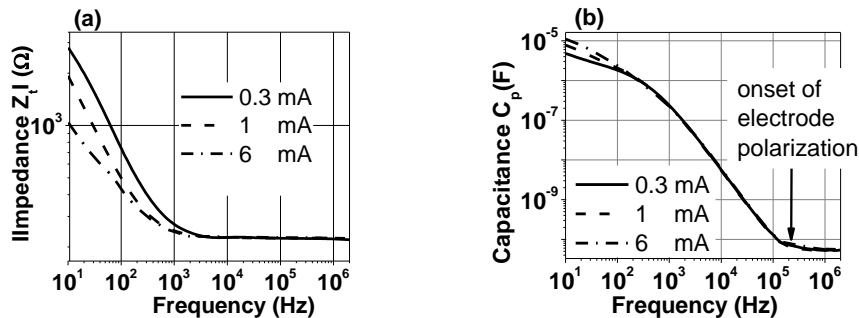


Fig. 4 – a) The impedance modulus $|Z_t(f,j)|$ measured with the DBS electrode in physiologic saline for three values of the current: 0.3, 1 and 6 mA (current density 5 to 100 mA cm^{-2}); b) The equivalent parallel capacitance $C_p(f,j)$ of the DBS electrode measured in the same conditions as above.

3.4. Monopolar Configuration

We measured the impedance when a stimulation voltage of 1 V was applied between E1 and an AgCl reference electrode. The results in Fig. 5 show that the impedance was smaller for monopolar configuration. The monopolar and bipolar impedances decreased with increasing f and above 3 kHz the decrease was insignificant.

3.5. The Coupling Capacitance Between the Leads and the Geometrical Capacitance Between Two Adjacent Contacts

The capacitance was constant (6.20×10^{-11} F, Fig. 3a) between 10 Hz and 2 MHz when the DBS electrode was in the air. The total impedance of the electrode in the air is characteristic for capacitive impedance:

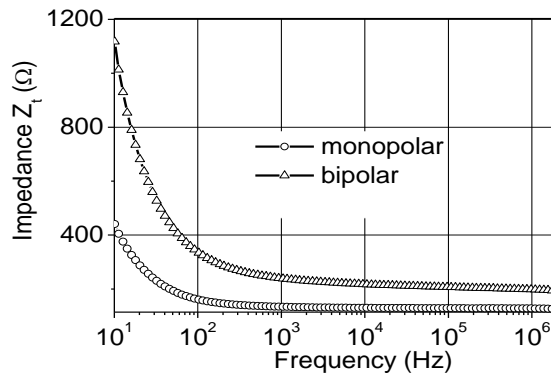


Fig. 5 – The absolute value of the impedance of the DBS electrode in 0.9% NaCl saline for the case of monopolar (circles) and bipolar (triangles) configuration. The applied voltage was 1V rms.

$$X_c = \frac{1}{\omega C_l} \quad (3)$$

where $\omega = 2\pi f$ is the angular frequency. Eq. (3) was used to fit the data from Fig. 3a and determine C_l . The capacitance in the air was $C_l = C_{le} + C_{cl} = (6.21 \pm 0.08) \times 10^{-11}$ F, similar to the result from Fig. 3a.

The real part of the dielectric permittivity of pure water is constant ($\epsilon' = 78$) for frequencies from 0 Hz to several GHz. Fig. 3a shows that for $f > 10$ kHz the capacitance was frequency independent with a value of 6.44×10^{-11} F. The capacitance of the contacts was estimated from the difference between the high-frequency capacitances (MHz range) in air and distilled water. The value was $C_{cl} = (3.1 \pm 0.9) \times 10^{-14}$ F. The capacitance of the two cylinders is very small compared to the coupling capacitance.

This conclusion is important for the use of electrode for EIS *in vivo*. The signal recorded *in vivo* depends on the capacitance of the contacts and the phenomena that take place at the metal-tissue interface. If the geometrical capacitance of the contacts is small, the recorded signal is small. This can result in a small Signal/Noise ratio, thus affecting data analysis.

3.6. Calculation of the Double Layer Capacitance and the Faradaic Resistance

For saline concentrations above 0.4%, the resistance decreased with increasing f and the variation was higher for higher NaCl concentrations (Fig. 3b). Above 1 kHz, the resistance was almost f independent and it is thought to reflect the saline resistance (Holsheimer *et al.*, 2000; Wei and Grill, 2009). The measured resistance has 2 components: R_l and R_s .

We used a fitting procedure (and the theoretical model) to determine the unknown parameters: $C_{dl0}(j)$, n , $R_{F0}(j)$ and m . The circles in Fig. 6a represent $Z_t(f)$ for 0.9% NaCl and 6 mA and the solid line is the best fit curve. The circles in Fig. 6b represent $C_p(f)$ for 0.9% NaCl and 6 mA and the solid line is the best fit curve.

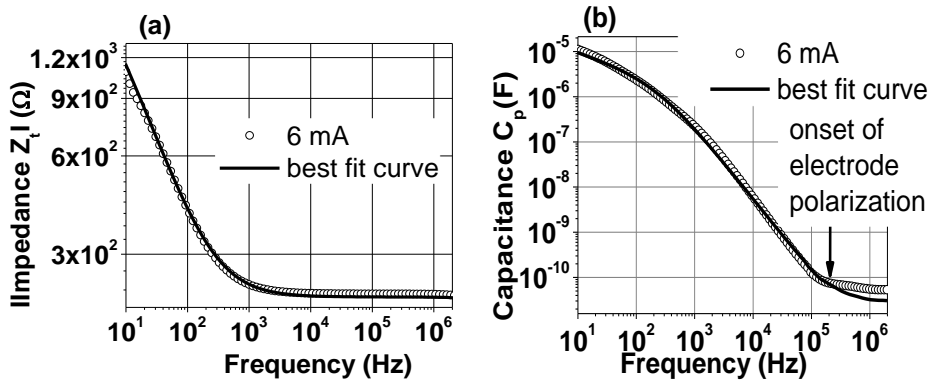


Fig. 6 – Typical fitting curves to determine the unknown parameters $C_{dl0}(j)$, n , $R_{F0}(j)$ and m .

The fit for $C_p(f)$ is less precise for $f > 0.3$ MHz. This may happen because at high f the coupling capacitance between the leads is the main capacitance and it is distributed along the leads. The data obtained for n and m are weakly but linearly dependent on logarithm of j . C_{dl0} and R_{F0} cannot be expressed as simple functions of j . When j decreases, C_{dl0} and n decrease and R_{F0} and m increase. C_{dl0} and n are less sensitive to j than R_{F0} and m . R_s was calculated using the geometry factor GF.

Table 1

The Values of C_{dl0} , n , R_{F0} and m obtained from the Fitting of the Experimental Data for Different j with the Proposed Model. The Relative Errors Affecting the Parameters are Below 7% for C_{dl0} and R_{F0} and Below 4% for n , m

j , [mA cm ⁻²]	C_{dl0} , [Fs ⁻ⁿ]	n	R_{F0} , [Ω s ^{-m}]	m
100	62.11 x10 ⁻⁶	0.360	5088	0.259
66.7	44.81 x10 ⁻⁶	0.341	8570	0.291
33.3	37.11 x10 ⁻⁶	0.309	14226	0.350
16.7	29.21 x10 ⁻⁶	0.291	22167	0.401
11.7	22.11 x10 ⁻⁶	0.272	34265	0.439
5	14.41 x10 ⁻⁶	0.250	55453	0.490

The data in Table 1 are in good agreement with the general behavior of C_{dl} and R_F at different current densities above the linearity limit (Ragheb and Geddes, 1990; Onaral and Schwan, 1983). Because the f range was large and the number of the unknown parameters deduced from the fitting procedure was low, the fitting procedure yielded unique values for the parameters. We know all the components of the equivalent circuit presented in Fig. 2b.

4. Discussion

Our goal was to provide an electrical model for DBS electrode impedance and to characterize the contact-saline impedance which is part of a complex electrical circuit. We made distinction between the saline solution, the metal-saline interface and other components related to DBS electrode design.

4.1. Model of the Equivalent Electric Circuit for the Interface Impedance

Previous studies modeled the DBS electrode interface with f independent lumped components (Holsheimer *et al.*, 2000), constant phase element (Lempka *et al.*, 2009) or an f and j dependent resistor in parallel with an f and j dependent capacitor (Wei and Grill, 2009). We make here a step further and show how $C_{dl}(f,j)$ and $R_F(f,j)$ change with f and j for therapy-relevant parameters. Eqs. (1) and (2) were used to quantify this variation (Onaral and Schwan, 1982; Geddes, 1997).

4.2. Electrical Efficiency of the DBS Electrode

We propose to use the ratio between the voltage drop on the saline and the stimulation voltage to characterize the electrical (energy) efficiency of the electrode during the stimulation process. The voltage U_{ap} generated by the stimulator will determine a current:

$$I(f) = \frac{U_{ap}}{|Z_t(f)|} \quad (4)$$

The voltage drop on saline is:

$$U_s(f) = I(f)R_s \quad (5)$$

The electrical efficiency $\eta(f)$ for a given current is:

$$\eta(f) = \frac{U_s(f)}{U_{ap}} = \frac{R_s}{|Z_t(f)|} \quad (6)$$

It reflects how much of the applied voltage will spread in the tissue and eventually contribute to stimulation. Eq. (6) is equally valid for constant current stimulation. Fig. 7 shows the electrical efficiency for three values of the current from 0.3 to 6 mA. The electrical efficiency was f dependent: it was low at low f , increased to 56% at 3 kHz and was constant at higher frequencies. For monopolar stimulation, when the implanted pulse generator is used as reference, the electrical impedance between the active contact and the reference was estimated at 1001Ω (Walckiers *et al.*, 2010). The smallest value of the resistance for the stimulated volume can be approximated with R_s yet the electrical efficiency of monopolar stimulation is low. The efficiency will drop further if other series resistances at the electrode-tissue interface are taken into account such as the encapsulation layer at the surface of the contact or the implanted pulse generator. Finding solutions to decrease R_t seems reasonable in order to increase the electrical efficiency of the DBS electrode.

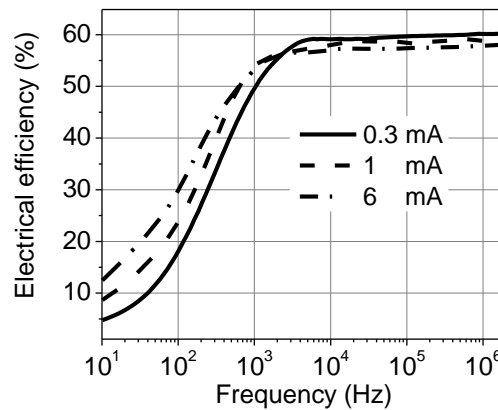


Fig. 7 – The electrical efficiency $\eta(f)$ for three values of the current. The electrical efficiency is frequency dependent.

4.3. Electric Charge Transfer at the Interface

The capacitive current determines a capacitive charge transfer ($Q_c(f)$) through the double layer capacitance and the resistive current determines a resistive charge transfer ($Q_F(f)$) through the faradaic resistance. Q_c/Q_F can be used to evaluate the tendency of the stimulation process to cause electrode or tissue damage. Using the proposed model, for a given current the above ratio can be written as:

$$\frac{Q_c(f)}{Q_F(f)} = \frac{I_c(f)}{I_F(f)} = \omega R_F C_{dl} = 2\pi R_{F0} C_{dl0} f^{1-m-n} \quad (7)$$

Data in Table 1 show that $m+n < 1$. For the whole data range in Table 1 $Q_c/Q_F > 4$, is j dependent and the ratio increases when f increase. The ratio Q_c/Q_F was relatively insensitive to frequency for $f < 10$ kHz (Wei and Grill, 2009). When C_{dl} and R_F were calculated the coupling capacitance between the leads was neglected and the saline impedance was taken equal with the asymptotic high frequency impedance of the DBS electrode (Wei and Grill, 2009).

4.4. Limitations

Our results showed that the DBS electrode impedance was selectively parameter-dependent. The electrical models are complex and the complexity varies based on parameters variability. A major difficulty in choosing a model is the interface impedance whose f dependence is different from that of a capacitor. Although there are many attempts to model the metal-saline interface, we hereby propose a new model. Results from a large range of experimental conditions can be analyzed with this model. The model must be further completed if it were to describe the electrode behavior for lower frequencies of stimulation (below 10 Hz). It is known that the interface is nonlinear at low frequencies. In this situation the analysis of the higher order harmonic response of a system to sinusoidal current or voltage perturbation is useful (Richardot and McAdams, 2002). For frequencies higher than 0.6 MHz, the DBS electrode cannot be used for tissue electrical properties measurements because of the coupling capacitance between the leads.

We did not take into consideration the spatial variation of the current density along the contact (Bard and Faulkner, 1980). The model can be further refined if it includes the effects related to the presence of an encapsulation layer.

4.5. Clinical Relevance of the Results

The electrode is used for therapy, but its use for electrophysiological characterization of the nervous tissue presents a particular interest. The current

passing through tissue for a stimulation voltage can be calculated accurately if the electrode impedance is known. This may facilitate a better selection of the stimulation parameters. The average value of the impedance determined in patients is about 1200 Ω (range: 415–1999 Ω) (Coffey, 2008). As a safety feature, the programming device calculates the charge density based on a conservative impedance value of 500 Ω . Our results showed that when the current varied from 0.3 to 6 mA the impedance varied between 600 and 400 Ω , when f varied from 50 to 300 Hz (Fig. 4a). For frequencies above 300 Hz the impedance was lower than 400 Ω . The clinical pulse repetition frequency range is between 130 and 185 Hz at pulse widths between 60 and 210 μs . This results in harmonics above 2.38 kHz and for this frequency range our results showed that the parameter of interest for stimulation programming, $Z_t(f,j)$ was practically j independent and f independent. The impedance was below the safety conservative impedance value and the electrode efficiency was about 56%. For a pulse duration of 200 μs the fundamental harmonic is 2.5 kHz. Data in Table 1 shows that the relaxation time at this f is 2.5 ms. If pulse repetition frequency is 185 Hz ($T = 5.4$ ms) the time between two pulses is too short for double layer capacitor discharging. Consequently charge balanced pulses (Coffey, 2008) are used to assure completely discharge of the double layer capacitor.

The ratio between the capacitive and resistive charge can be calculated using Eq. (7) and data in Table 1 and can be used to evaluate the tendency of the stimulation process to cause electrode or tissue damage.

We evaluate here the coupling capacitance between the leads and the geometrical capacitance between two adjacent contacts. They are important in understanding the upper f limit for electrode use to EIS measurements *in vivo*.

5. Conclusions

We proposed a model for the DBS electrode and contact-saline interface which accounts for the nonlinear dependence of $R_F(f,j)$ and $C_{dl}(f,j)$ with f and j . The impedance of the DBS electrode decreased when the applied voltage increased. The voltage dependence became less important with increasing frequency. For frequencies higher than 3 kHz the impedance was independent of the applied voltage (0.3 – 1 V rms) or j (5 to 100 mA cm^{-2}), and it was below the safety conservative impedance value. The electrical (energy) efficiency of stimulation was f dependent and about 56% above 3 kHz for bipolar stimulation and lower for monopolar stimulation. The relaxation time of charge accumulated at the interface is 0.8 to 100 times the signal period indicating that the relaxation of the charge accumulated in the double layer is a slow process.

The geometrical capacitance of the active part of the DBS electrode was very low compared with the coupling capacitances C_{le} between the metallic wires. Consequently, a change of the dielectric properties of the medium around the electrode will determine a weak change of the collected signal.

REFERENCES

- Ackmann J.J., Seitz A.S., *Methods of Complex Impedance Measurements in Biological Tissue*, CRC Crit. Rev. Biom. Eng., **10**, 281-311 (1984).
- Bard A.J., Faulkner L.R., *Electrochemical Methods: Fundamentals and Applications*, New York, Wiley, 1980.
- Butson C.R., McIntyre C.C., *Tissue and Electrode Capacitance Reduce Neural Activation Volumes During Deep Brain Stimulation*, Clin. Neurophysiol., **116**, 2490-500 (2005).
- Coffey R.J., *Deep Brain Stimulation Devices: A Brief Technical History and Review*, Artificial Organs, **33**, 208-220 (2008).
- Cogan S.F., *Neural Stimulation and Recording Electrodes*, Annu. Rev. Biomed. Eng., **10**, 275-309 (2008).
- Geddes L.A., *Historical Evolution of Circuit Models for the Electrode-Electrolyte Interface*, Ann. Biomed. Eng., **25**, 1-14 (1997).
- Geddes L.A., DaCosta C.P., Wise G., *The Impedance of Stainless-Steel Electrodes*, Med. & Biol. Eng., **9**, 511-521 (1971).
- Holsheimer J., Dijkstra E.A., Demeulemeester H., Nuttin B., *Chronaxie Calculated from Current-Duration and Voltage-Duration Data*, J. Neurosci. Method, **97**, 45-50 (2009).
- Lempka S., Miocinovic S., Johnson M.D., Vitek J.L., McIntyre C.C., *In Vivo Impedance Spectroscopy of Deep Brain Stimulation Electrodes*, J. Neural Eng., **6**, 321-332 (2009).
- McAdams E.T., Jossinet J., *Tissue Impedance—a Historical Overview*, Physiol. Meas., **16**, A1-3 (1995).
- McCreery D.B., Agnew W.F., Yuen T.G., Bullara L., *Charge Density and Charge per Phase as Cofactors in Neural Injury Induced by Electrical Stimulation*, IEEE Trans. Biomed. Eng., **37**, 996-1001 (1990).
- Macdonald J.R., *Impedance Spectroscopy*, Ann. Biomed. Eng., **20**, 289-305 (1992).
- McIntyre C.C., Mori S., Sherman D.L., Thakor N.V., Vitek J.L., *Electric Field and Stimulating Influence Generated by Deep Brain Stimulation of the Subthalamic Nucleus*, Clin. Neurophysiol., **115**, 589-595 (2004).
- Miocinovic S., Lempka S.F., Russo G.S., Maks C.B., Butson C.R., Sakaie K.E., Vitek J.L., McIntyre C.C., *Experimental and Theoretical Characterization of the Voltage Distribution Generated by Deep Brain Stimulation*, Exp. Neurol., **216**, 166-176 (2009).
- Onaral B., Schwan H.P., *Linear and Nonlinear Properties of Platinum Electrode Polarization, Part I: Frequency Dependence at Very Low Frequencies*, Med. Biol. Eng. Comput., **20**, 299-305 (1982).
- Onaral B., Schwan H.P., *Linear and Nonlinear Properties of Platinum Electrode Polarization. Part 2: A Time Domain Analysis*, Med. Biol. Eng. Comput., **21**, 210-216 (1983).
- Ragheb T., Geddes L.A., *Electrical Properties of Metallic Electrodes*, Med. Biol. Eng. Comput., **28**, 182-186 (1990).
- Richardot A., McAdams E.T., *Harmonic Analysis of Low-Frequency Bioelectrode Behavior*, IEEE Trans. Biomed. Imaging, **21**, 604-613 (2002).

- Schwan H.P., Maczuk J.G., *Electrode Polarization Impedance: Limits of Linearity*, Proc. 18th Ann. Conf. Eng., In Med. & Biol., 1965.
- Schwan H.P., *Electrode Polarization Impedance and Measurements in Biological Materials*, Ann. NY Acad. Sci., **148**, 191-209 (1968).
- Shepherd R.K., Clark G.M., *Scanning Electron Microscopy of Platinum Scala Tympani Electrodes Following Chronic Stimulation in Patients*, Biomaterials, **12**, 417-423 (1991).
- Walckiers G., Fuchs B., Thiran J.P., Mosig J.R., Pollo C., *Influence of the Implanted Pulse Generator as Reference Electrode in Finite Element Model of Monopolar Deep Brain Stimulation*, J. Neurosci. Methods, **186**, 90-96 (2010).
- Wei X.F., Grill W.M., *Impedance Characteristics of Deep Brain Stimulation Electrodes in Vitro and in Vivo*, J. Neural Eng., **6**, 4, 046008 (2009).

CARACTERIZAREA IMPEDANȚEI ELECTRODULUI PENTRU STIMULARE
PROFUNDĂ ÎN CREIER: SPECTROSCOPIE
DE IMPEDANȚĂ ELECTROCHIMICĂ ÎN CURENT ALTERNATIV

(Rezumat)

Impedanța electrodului pentru stimulare profundă în creier (DBS) Medtronic 3387 este caracterizată folosind spectroscopia de impedanță electrochimică (EIS). Interfața metal-soluție salină a fost modelată ca un circuit paralel format din rezistența $R_F(f,j)$ și capacitatea stratului dublu $C_{dl}(f,j)$. Modelul ia în considerare dependența lui $R_F(f,j)$ și $C_{dl}(f,j)$ de frecvența f și densitatea de curent j . În model a fost inclusă și capacitatea parazită dintre firele metalice care fac legătura între cilindri și conector. $C_{dl}(f,j)$ și $R_F(f,j)$ au fost determinate din fitarea modelului teoretic cu datele experimentale. Se arată că există o importantă cădere de tensiune la interfață care afectează distribuția tensiunii de stimulare în creier. Randamentul electric al electrodului este mic pentru frecvențe joase, crește la 56% la 3 kHz și rămâne constant la frecvențe mai mari.

BULETINUL INSTITUTULUI POLITEHNIC DIN IAȘI
Publicat de
Universitatea Tehnică „Gheorghe Asachi” din Iași
Volumul 62 (66), Numărul 3, 2016
Secția
MATEMATICĂ. MECANICĂ TEORETICĂ. FIZICĂ

INFLUENCE OF COMBUSTION AGENTS AND THERMAL TREATMENT ON PROPERTIES OF IRON MANGANESE OXIDES

BY

ELENA VASILICA GAFTON^{1,*}, GEORGIANA BULAI¹, IOAN DUMITRU¹,
FLORIN TUDORACHE¹, OVIDIU F. CĂLȚUN¹, ADRIAN IULIAN BORHAN²,
ALEXANDRA RALUCA IORDAN² and MIRCEA NICOLAE PALAMARU²

“Alexandru Ioan Cuza” University of Iași,

¹Faculty of Physics

²Faculty of Chemistry

Received: November 19, 2016

Accepted for publication: December 17, 2016

Abstract. Nanocrystalline iron manganese oxides with cubic structure were synthesized by autocombustion method using different fuel agents and annealing treatments. The synthesized samples were characterized by X-ray diffraction, vibrating sample magnetometry and electric measurements. The X-Ray analysis indicated that the phase content after combustion and in different stages of the thermal treatment is influenced by the type of fuel agent used in the synthesis process. The crystallite size of the obtained samples was found to be in nanoscale range. The specific saturation magnetization and the coercive field measurements confirmed the identification of the phase content. The permittivity and electrical resistivity measurements done on the powders obtained using hexamethylenetetramine, urea, and citric acid as combustion agents recommend the use of these samples for humidity sensor applications.

Keywords: nanostructures; sol-gel chemistry; X-ray diffraction; Rietveld analysis; humidity sensor.

*Corresponding author; *e-mail*: gafton.vasilica@gmail.com

1. Introduction

Polycrystalline oxides with general formula $A^{II}B^{III}O_3$, which have an inorganic chameleon due to the large flexibility of the structure (Hamdad, 2011) have drawn attention of researchers because of various applications. These materials can act as efficient heterogeneous catalysts (Watanabe *et al.*, 2015) (Su *et al.*, 2014), sensors (Ghasdi and Alamdari, 2010; Fergus, 2007), electrode materials for solid oxide fuel cells (Zhong *et al.*, 2005) and gas storage (Xian *et al.*, 2010; Chen *et al.*, 2015).

Although $FeMnO_3$ properties were investigated by several research groups (Sfeir *et al.*, 2005; Rayaprol *et al.*, 2013; Seifu *et al.*, 2000; Herranz *et al.*, 2006; Leith *et al.*, 1988), only a few applications have been reported. Li *et al.* studied electrochemical energy storage performances of supercapacitor based on $FeMnO_3$ hollow sphere/graphene composites. They reported that the obtained $FeMnO_3$ perovskite displays improved crystallization and different morphologies as the calcination temperature is increased (Li *et al.*, 2014). Kulshreshtha *et al.* reported catalytic CO oxidation over γ - $FeMnO_3$ after palladium addition (Kulshreshtha *et al.*, 2004). Rezlescu *et al.* prepared $FeMnO_3$ perovskite by sol-gel self-combustion method and tested the samples for catalytic combustion of dilute acetone in air. The acetone conversion degree over perovskite catalysts exceeded 95% at 300°C (Rezlescu *et al.*, 2015). Doroftei *et al.* studied the catalytic activity of the nanocrystalline $FeMnO_3$ for the combustion of acetone vapors and of some hydrocarbons diluted in air. The authors reported that the obtained perovskite is a good catalyst for gas and vapor combustion (Doroftei *et al.*, 2014). Also, $FeMnO_3$ shows high capacity, excellent rate capability, and good cycling stability when used as electrode for Li batteries (Cao *et al.*, 2016).

Our main objective was to synthesize pure nanocrystalline iron manganese oxide powders by sol-gel auto-combustion method and to investigate the influence of chelating/combustion agents on the structural features and magnetic properties by using, for the first time, five different chelating/combustion agents. As far as we know, no other papers reported the combined effect of different chelating/fuel agents on the structural, magnetic and sensing properties of $FeMnO_3$. The influence of different chelating/combustion agents on structural and physical properties of spinel oxides is related to their different interactions with the reactants, changing the morphology and crystallinity of the resulting powders (depending on the amount of generated heat) (Druc *et al.*, 2013). The effectiveness of magnetic materials used in sensor applications depends on the microstructural and magnetic properties of starting powders. The raw materials are very sensitive to the preparation conditions of sol-gel autocombustion method (Slatineanu *et al.*, 2011). This method offers specific advantages in preparations of multi-component

oxide materials, such as: stoichiometric control of simple reactants, reduced synthesis time, good chemical homogeneity and nanometric size of the particles.

The novelty of this research consists in preparation of iron manganese oxide fine particles with various average size using different combustion agents for further application as humidity sensors. The particle size and phase content were controlled by changing the type of fuel agent which imposes different reaction speeds and temperatures. The influence of post annealing processes applied to achieve the desired phase was also studied. Detailed investigations of the structure and magnetic properties were done in order to understand the evolution from precursor solutions to the final powders.

2. Experimental Details

FeMnO_3 nanoparticles were prepared by sol-gel auto-combustion method. Analytical grade manganese nitrate, $[\text{Mn}(\text{NO}_3)_2 \cdot 4\text{H}_2\text{O}]$ (Aldrich) and iron nitrate (III), $[\text{Fe}(\text{NO}_3)_3 \cdot 9\text{H}_2\text{O}]$ (Aldrich) were mixed in stoichiometric proportions with different chelating/combustion agents such as: tartaric acid (99.9%, Aldrich) (AT), citric acid (99.9%, Merck) (AC), urea (99.9%, Merck) (U), glycine (99.9%, Merck) (Gly), and hexamethylenetetramine (99%, Merck) (Hex). Fig. 1 illustrates the reaction process that takes place during nanopowder synthesis. Reagents were dissolved in distilled water forming one solution for each chelating/combustion agent. Then fuel agents were added to each sample of metal nitrates mixture in 1:1 molar ratio of fuel agent: metallic cations. After synthesis step, the solutions were heated at 75°C through gel phase transformation and then naturally cooled down to room temperature to obtain dry gel. The gels were gradually heated at 300°C , during which autocombustion occurred (Slatineanu *et al.*, 2011). The samples were labelled as MF_AT, MF_AC, MF_U, MF_Gly and MF_Hex.

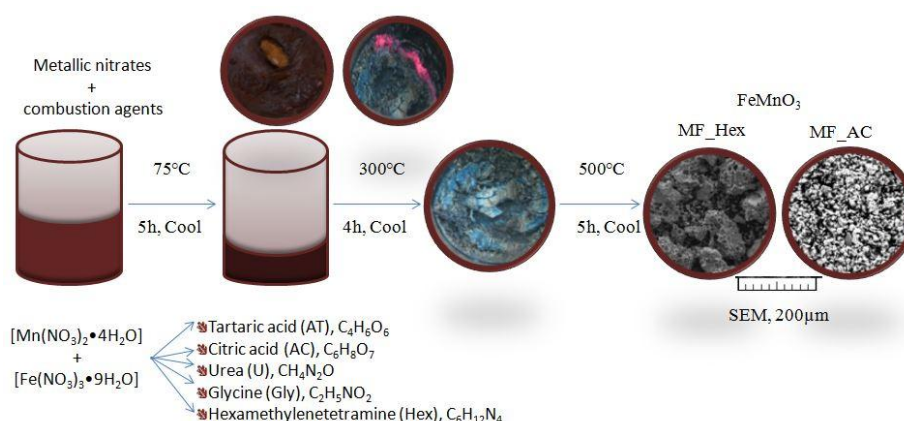


Fig. 1 – An illustrated sol-gel combustion method process for the synthesis of FeMnO_3 .

To understand the process dynamics, the as-synthesized powders were micro-structurally and magnetically characterized. After a first phase content analysis of the powders annealed at 500°C for 5 h a subsequent thermal treatment was done at 900°C for 7h. Part of as-synthesized powders was directly calcined at 1200°C for 4h in air. The phase content and magnetic properties were checked at every synthesis step. X-ray diffraction (XRD) was performed using a Shimadzu LabX XRD-6000 (Cu $K\alpha$ radiation, $\lambda = 1.5405 \text{ \AA}$) with 2θ ranging between 20° and 90° and 0.02° scanning rate. Magnetic measurements were performed at room temperature using a vibrating sample magnetometer system (Model VSM 3900 Princeton). Electrical properties were studied using an Agilent E4980A Precision LCR Meter-type impedance analyzer. Permittivity and electrical resistivity measurements, in the frequency range of 20 Hz - 107 Hz, were performed in parallel-plate capacitor configuration, by applying Pd – Ag electrodes on the polished surfaces of the FeMnO₃ disks (6 mm diameter, 2 mm thickness) obtained by pressing. The influence of humidity on the electrical properties was analyzed by placing the samples into a closed box at 23°C with controlled humidity between 0% and 100% RH.

3. Results and Discussion

3.1. Structural Analysis

The XRD patterns of the iron manganese oxides calcined at 500°C are shown in Fig. 2a. All the identified peaks were indexed in good agreement with the referred ICDD cards (* * ICDD). The results revealed the presence of α -Fe₂O₃ (antiferromagnetic) and FeMnO₃ (ferrimagnetic) phases in different ratios. Phases content for each sample and lattice parameters determined from Rietveld analysis are reported in Table 1. One can observe that the combustion agent has a significant influence on α -Fe₂O₃ phase content which varies from 20.89% in MF_Hex to 94.2% in MF_U.

A further thermal treatment of the powders at higher temperature was performed at 900°C. As one can observe from the diffraction patterns presented in Fig. 2b, the α -Fe₂O₃ phase increases, but a small amount of FeMnO₃ still exist. Phase content analysis of samples calcined directly at 1200°C demonstrated that high temperatures favor the formation of FeMnO₃ (ferrimagnetic structure at room temperature) accompanied by a low percentage of MnFe₂O₄ (ferrimagnetic spinel structure). The highest ratio of spinel phase content of 4% corresponds to MF_U sample.

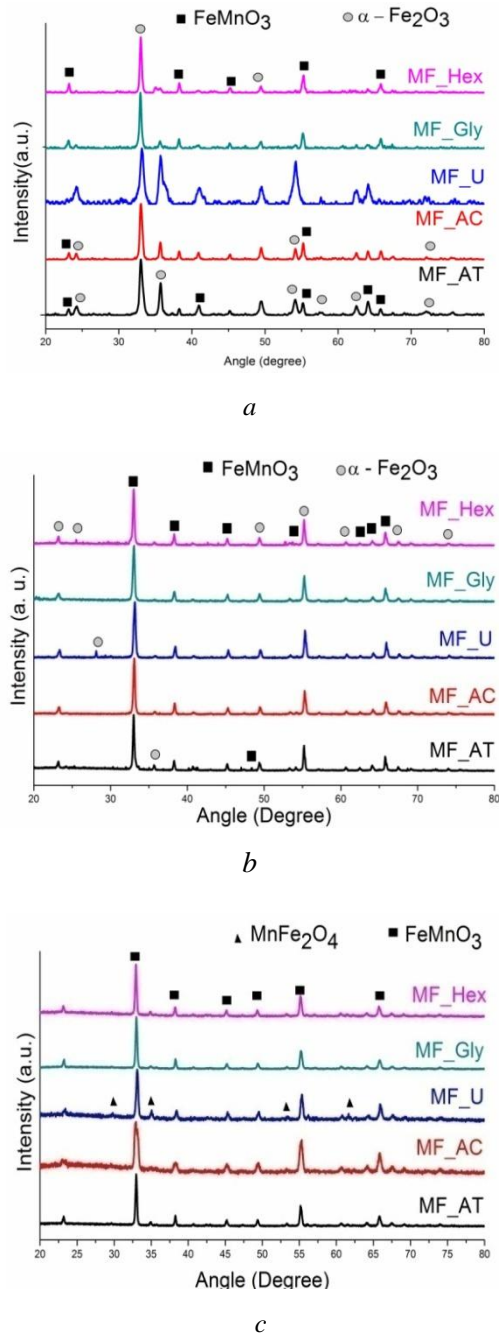


Fig. 2 – XRD patterns (color online) of iron manganese oxides powders synthesized with different agents and annealed at different temperatures: *a*) 500°C, *b*) 900°C and *c*) 1200°C.

Table 1
Phase Content of Samples Annealed at Different Temperatures. GofF
Represents the Goodness of Fit

	°C	MnFe ₂ O ₄		α-Fe ₂ O ₃			FeMnO ₃		GofF
		%	a	%	a	c	%	a	
MF_AT	500			71.56	5.03(2)	13.7596(3)	28.44	9.4057(1)	1.09
	900			15.73	5.3089(6)	13.4737(3)	84.27	9.4175(9)	1.82
	1200	1.41	8.5266(5)				98.59	9.4139(1)	1.45
MF_AC	500			44.9	5.0336(4)	13.4734(5)	55.1	9.408(7)	1.06
	900			6.65	5.3068(1)	13.7453(7)	93.35	9.4119(7)	1.34
	1200	0.31	8.6378(6)				99.69	9.4073(5)	1.62
MF_U	500			94.2	5.9267(5)	13.7754(4)	5.8	9.6082(9)	1.17
	900			4.34	5.0419(1)	13.7609(8)	95.66	9.4166(7)	1.54
	1200	4.03	8.5343(6)				95.97	9.4212(9)	1.38
MF_Gly	500			35.3	5.0293	13.775(2)	64.7	9.4057(1)	1.1
	900			1.02	5.0344(7)	13.7945(3)	98.98	9.4142(5)	1.36
	1200	0.44	8.1595				99.56	9.4131(3)	1.47
MF_Hex	500			20.89	5.0475(6)	13.72	76.36	9.4024(8)	1.17
	900			3.46	5.3094	13.7558(5)	96.54	9.1347(5)	1.76
	1200	1.85	8.5257(1)				98.15	9.4138(6)	1.39

The broad XRD lines indicate that crystallites are in nanosize scale. The crystallite sizes listed in Table 2 were calculated from 222 peak broadening found at $2\theta \approx 33^\circ$ using Debye-Scherrer formula: $D = \frac{0.89 \cdot \lambda}{\beta \cdot \cos \theta}$, where D is the crystallite size, λ is the wavelength of X-ray used, β (rad) is the full width at half maximum of the diffraction peak and θ is the diffraction angle. The highest value of 41 nm was observed for MF_AT sample calcined at 900°C.

Table 2
Crystallites Size in Nanometers of FeMnO₃ Powders Thermally
Treated from X-ray Diffraction Patterns

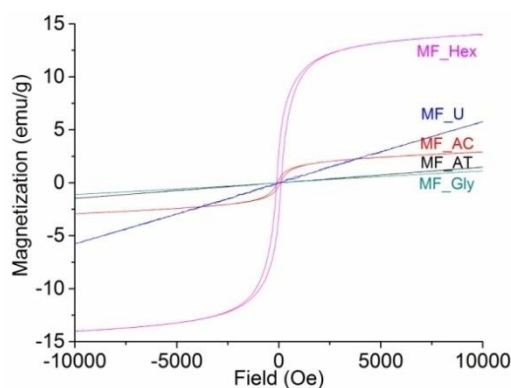
FeMnO ₃	AT	AC	U	Gly	Hex
500°C	18	21	15	28	27
900°C	41	34	28	29	35
1200°C	36	15	29	35	35

The average crystallite size is strongly influenced by the intensity of the combustion reaction. Combustion induced by tartaric acid is the less intense (Dumitrescu *et al.*, 2013) and it explains the larger crystallite size than in the

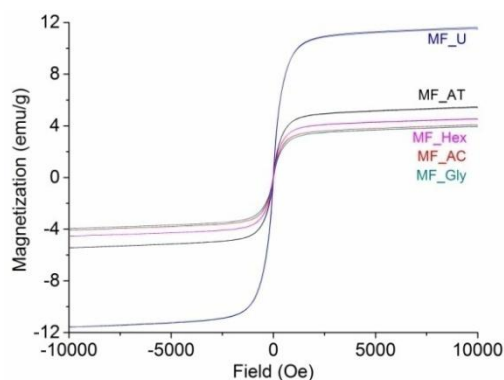
other cases. Usually, high annealing temperature increases the particle size due to Oswald ripening (Zeng, 2007).

3.2. Magnetic Properties

Magnetizations (M) versus magnetic field (H) hysteresis loop measured at room temperature are presented in Fig. 3 and the values of the magnetic parameters are listed in Table 3. Magnetic properties of nanoparticles are influenced by the phase content and average particles size. The shape of the curves for the powders calcined at 500°C and synthesized using hexamethylenetetramine and citric acid as combustion agents have higher magnetization values, which can be explained by the higher FeMnO_3 phase percentage determined from XRD patterns.



a



b

Fig. 3 – Magnetization as a function of applied field loops of FeMnO_3 powders sintered at: *a*) 500°C and *b*) 1200°C .

For powders corresponding to same annealing temperatures, the higher magnetization is due to the higher percentage of the magnetic phase. The use of different fuel agents influences the geometrical arrangement of the different cations and the resulting magnetic coupling.

Table 3
Magnetic Parameters of FeMnO₃ Powders

FeMnO ₃	M _S (emu/g)		H _C (Oe)	
	500°C	1200°C	500°C	1200°C
MF_AT	0.4	5.4	--	11
MF_AC	0.7	4.1	70	14
MFU	0.3	11.1	--	12
MF_Gly	2	3.9	--	20
MF_Hex	9	4.4	109	15

MF_Hex powder calcined at 500°C, with $D_{cryst} = 27$ nm, exhibits the largest values of coercivity, 109 Oe, and specific magnetization, 10.7 emu/g. The powders prepared with urea and tartaric acid appears to be paramagnetic at room temperature, observation that can be correlated to the large ratio of α -Fe₂O₃ identified in XRD patterns. The values of saturation magnetization for the powders thermally treated at 1200°C are generally higher compared with the samples calcined at 500°C. These values ranging between 4 and 11 emu/g correspond to the FeMnO₃ phase and are comparable with ones reported in literature (Rayaprol *et al.*, 2013). For example, in case of MF_U, a crystalline FeMnO₃ and MnFe₂O₄ phase was formed at 1200°C, leading to a magnetization increase to 10 emu/g. In addition, a small increase in the magnetic properties can be attributed to the increase in crystallite size for all materials from 15 nm at 500°C to 36 nm at 1200°C. This behavior indicates a direct relationship between magnetic properties and crystal growth as observed by Zhang *et al.* in their study on MnFe₂O₄ obtained by coprecipitation (Zhang and Nan, 2015).

3.3. Electrical Properties under Humidity Influence

In order to use the materials as humidity sensors, their electrical properties are relevant. The relative permittivity and electrical resistivity are mainly dependent on the ion exchange mechanism between ions from different positions, corresponding to typical cubic structures. As shown in Figs. 4 and 5, the relative permittivity and electrical resistivity of all samples decrease with the frequency in the relative humidity range 0–100% RH, in accordance with typically Maxwell–Wagner type interfacial polarization (Jawada *et al.*, 2012).

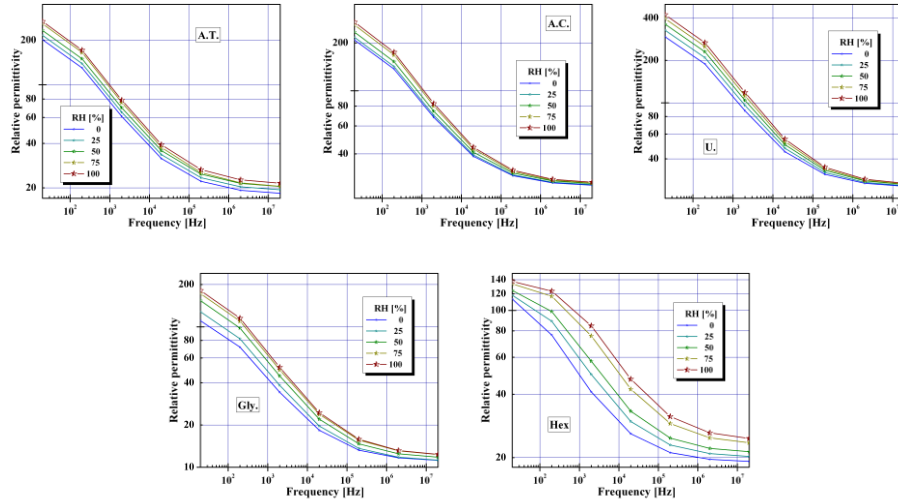


Fig. 4 – Frequency dependence of the relative permittivity at room temperature in the relative humidity range 0–100%.

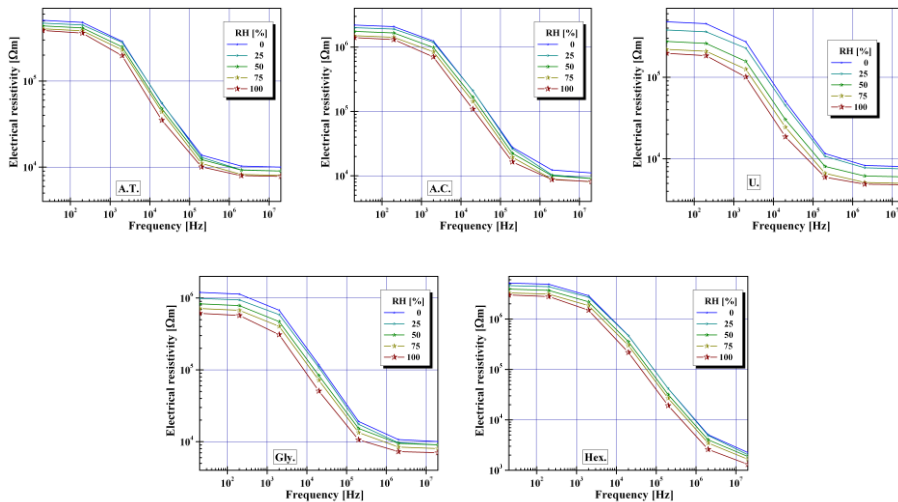


Fig. 5 – Variation of electrical resistivity with frequency in presence of water vapors.

According to this theory, the conductivity of grain boundaries contributes more to the relative permittivity at lower frequencies. Normally, with increasing of annealing temperature, there is an increase of relative permittivity and a decrease of electrical resistivity due to the formation of grains

with high conductivity (Petřila and Tudorache, 2013). Therefore, we have investigated the electrical properties of the cubic type oxides annealed at 900°C, because the high values of electrical resistivity hinder the use as materials for humidity sensors, although its sensitivity to humidity is high. The difference between the values of electrical resistivity indicates that the use of urea as fuel agent is favorable. Instead, the use of the hexamethylenetetramine (Hex) as chelating/combustion agent lead to the formation of secondary phases which occur due to short combustion time and high temperature during combustion (Druc *et al.*, 2013). However, the resistivity of all materials prepared is brought into the measurable zone, useful for sensors applications.

At 20 Hz, the relative permittivity values of MF_U and MF_Hex samples at 100% relative humidity are 400 and 140, respectively. The rest of materials have the permittivity almost equal to 200. The variation of permittivity response depending on the frequency is strongly influenced by the crystallinity, porosity, grain size, and pore-size distribution within the microstructure (Muthu and Lakshminarasimhan, 2013). Hence, this variation can be attributed to the structural changes caused by fuel agents. The humidity, as expected, produces an increase in permittivity and a decrease in resistivity of the materials, because of open pores filling with water vapors. It can be observed that for low relative humidity, all samples possess high electrical resistivity values, which decreases with increasing of RH, [%]. Therefore, the humidity influence on the relative permittivity and electrical resistivity function of frequency can be attributed to the Maxwell–Wagner Debye relaxation in the case of the vapors that fill the materials pores (Tudorache *et al.*, 2013) However, it is interesting that for MF_U was obtained the lowest value of electrical resistivity. This could be related to the long time of the auto-combustion process, allowing stabilization of the structure. Another reason could be the occupation of the lattice positions by the ions. The results indicate large variations of permittivity and electrical resistivity under humidity of prepared samples, and recommend that these materials can be used as humidity sensors. In this respect, the sensitivity to humidity can be highlighted by the capacitive or resistive humidity sensitivity coefficients. In Fig. 6(a-b) the capacitive and resistive humidity sensitivity coefficients of sensors in function of relative humidity based on iron manganese oxides are represented. As can be seen, the sensitivity of both resistive and capacitive sensors is increased with increase of the temperature treatment mainly due to the microstructure and pore size distribution. All the sensors exhibit S_R smaller than 60%, and started to respond for extremely low RH values (of about 2%). It is worth to note that the device based on MF_U oxide showed higher S_R (about 58%), but the onset for all materials did not change.

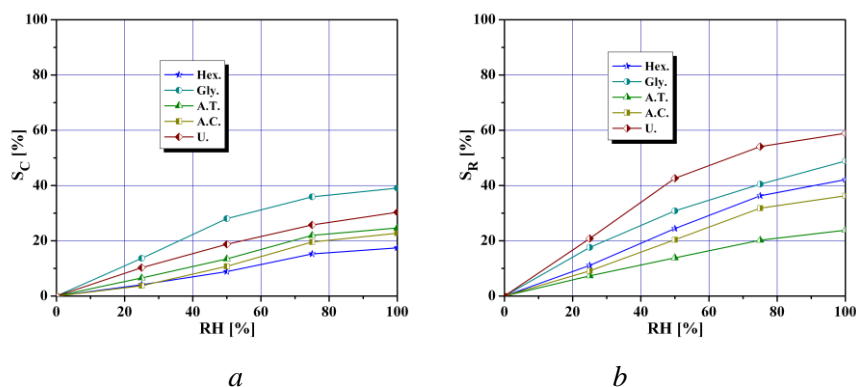


Fig. 6 – Humidity sensitivity characteristics of iron manganese material: a) Capacitive humidity sensitivity dependence on relative humidity; b) Resistive humidity sensitivity dependence on relative humidity.

According to literature, the chemisorption in oxides can be discarded at higher humidity levels, while physical adsorption takes place in the whole range of relative humidity and the time required to reach equilibrium is the time necessary for the H₂O pressure to establish into the various parts of the materials (Cavalieri *et al.*, 2012). At room temperature, the resistance humidity coefficient is mainly determined by the grain boundary resistance of the MF oxides. Taking this into account, the mechanism could consist in water adsorption, when a few water vapors tend to chemically adsorb on the grain surfaces of the oxide oxides giving rise to M–OH hydroxyl groups (Jing-Li *et al.*, 1991). Then, if more water vapor is adsorbed, liquid-like multilayer of hydrogen-bonded water molecules is formed, which condense into mesopores. Therefore, the dominant charge carriers in the water adsorbed in the mesopores are H⁺ protons, which increase with increasing the moisture content. Protons H⁺ can move freely in liquid water, giving a decrease of grain surface resistance with increasing relative humidity RH. This mechanism explains why electrical resistivity decreases with increasing relative humidity RH, leading to an increase of sensitive response S_R (Viviani *et al.*, 2001). In contrast to the resistive coefficient, the capacitive increases with increasing relative humidity RH, because the capacitance reflects the dielectric property of the MF oxides. Since water vapor molecules can be highly polarized, the accumulation of water on the grain surface of the MF samples increases the dielectric coefficient of the sensors.

3. Conclusions

Iron manganese oxides powders were synthesized by autocombustion method using five different combustion agents. The combustion fuels strongly influenced the phase composition. The FeMnO₃ percentage varied from 6% (for

MFU) to 76% (for MF_Hex) in the case of the powders calcined at 500°C. As a result the magnetic behavior changed from a paramagnetic state (MFU and MF_AT) to a ferrimagnetic one (MF_Hex and MF_AC). For the powders calcined at 1200°C the main observed phase was a ferrimagnetic oxide accompanied by small percentages of manganese ferrite. The highest saturation magnetization value of 11 emu/g was observed for MFU sample which also presented the highest percentage of manganese ferrite phase. MF perovskites exhibit large variations of permittivity and electrical resistivity under humidity influence, suggesting possible application as humidity sensors.

Acknowledgements. I. Dumitru acknowledges the support given by Romanian CNCS-UEFISCDI, project number PN-II-RU-TE-2012-3-0449.

REFERENCES

- Cao K. *et al.*, *FeMnO₃: a High-Performance Li-Ion Battery Anode Material*, Chem. Commun., Vol. **52**, 11414-11417 (2016).
- Cavalieri A. *et al.*, *Electrical Characterization of Room Temperature Humidity Sensors in La_{0.8}Sr_{0.2}Fe_{1-x}Cu_xO₃ (x = 0, 0.05, 0.10)*, Ceram. Int., Vol. **38**, 2865-2872 (2012).
- Chen C.-F. *et al.*, *Oxygen-Deficient BaTiO_{3-x} Perovskite as an Efficient Bifunctional Oxygen Electrocatalyst*, Nano Energy, Vol. **13**, 423-432 (2015).
- Doroftei C. *et al.*, *Structural and Catalytic Characterization of Nanostructured Iron Manganite*, Composites Part. B, Vol. **67**, 179-182 (2014).
- Druc A.C. *et al.*, *Optimization of Synthesis Conditions and the Study of Magnetic and Dielectric Properties for MgFe₂O₄ Ferrite*, Cent. Eur. J. Chem., Vol. **11**, 8, 1330-1342 (2013).
- Dumitrescu A.M. *et al.*, *Study of the Chelating/Fuel Agents Influence on NiFe₂O₄ Samples with Potential Catalytic Properties*, Powder Technology, Vol. **243**, 9-17 (2013).
- Fergus J.W., *Perovskite Oxides for Semiconductor-Based Gas Sensors*, Sens. Actuators, Vol. **B 123**, 1169-1179 (2007).
- Ghasdi M., Alamdari H., *CO Sensitive Nanocrystalline LaCoO₃ Perovskite Sensor Prepared by High Energy Ball Milling*, Sens. Actuators, Vol. **B 148**, 478-485 (2010).
- Hamdad N., *The Ground States Properties and the Spin Effect on the Cubic and Hexagonal Perovskite Manganese Oxide BaMnO₃: GGA+U Calculation*, Physica B, Vol. **406**, 1194-1203 (2011).
- Herranz T. *et al.*, *Synthesis, Structural Features, and Reactivity of Fe-Mn Mixed Oxides Prepared by Microemulsion*, Chem. Mater., Vol. **18**, 9 (2006).
- Leith I.R., Howden M.G. *Temperature-Programmed Reduction of Mixed Iron-Manganese Oxide Catalysts in Hydrogen and Carbon Monoxide*, Appl. Catal. A-Gen., Vol. **37**, 75-92 (1988).
- Jawada A.S. *et al.*, *Exploring the Dielectric Behaviour of Nano-Structured Al³⁺ Doped BiFeO₃ Ceramics Synthesized by Auto Ignition Process*, J. Alloys Compd., Vol. **530**, 25, 63-70 (2012).

- Jing-Li Z. *et al.*, *Electrical Conduction of $La_{1-x}Sr_xFeO_3$ Ceramics under Different Relative Humidities*, *Sens. Actuators A: Phys.*, Vol. **29**, 43-47 (1991).
- Kulshreshtha S.K. *et al.*, *CO Oxidation Over Pd/ $-FeMnO_3$ Catalyst*, *Indian J. Chem. Technol.*, Vol. **11**, 427-433 (2004).
- Li M. *et al.*, *Facile Synthesis of Specific $FeMnO_3$ Hollow Sphere/Graphene Composites and their Superior Electrochemical Energy Storage Performances for Supercapacitor*, *J. Power Sources*, Vol. **248**, 465-473 (2014).
- Muthu K.S., Lakshminarasimhan N., *Impedance Spectroscopic Studies on $NiFe_2O_4$ with Different Morphologies: Microstructure vs. Dielectric Properties*, *Ceram. Int.*, Vol. **39**, 2309-2315 (2013).
- Petrila I., Tudorache F., *Humidity Sensor Applicative Material Based on Copper-Zinc-Tungsten Spinel Ferrite*, *Mater. Lett.*, Vol. **108**, 129-133 (2013).
- Rayaprol S. *et al.*, *Structure and Magnetism of $FeMnO_3$* , *AIP Conf. Proc.*, Vol. **1512**, 1132 (2013).
- Rayaprol S. *et al.*, *Structure and Magnetism of $FeMnO_{3n}$* , *Proceedings of the 57th Dae Solid State Physics Symposium 2012, Solid State Physics*, AIP Publishing, 2013, Vol. **1512**.
- Rezlescu N. *et al.*, *Some Nanograined Ferrites and Perovskites for Catalytic Combustion of Acetone at Low Temperature*, *Ceram. Int.*, Vol. **41**, 4430-4437 (2015).
- Seifu D. *et al.*, *Evidence of Ferrimagnetic Ordering in $FeMnO_3$ Produced by Mechanical Alloying*, *J. Magn. Magn. Mater.*, Vol. **212**, 1-2 (2000).
- Sfeir J. *et al.*, *Characterization of Perovskite Powders for Cathode and Oxygen Membranes Made by Different Synthesis Routes*, *J. Eur. Ceram. Soc.*, Vol. **25**, 1991-1995 (2005).
- Slatineanu T. *et al.*, *Synthesis and Characterization of Nanocrystalline Zn Ferrites Substituted with Ni*, *Mater. Res. Bull.*, Vol. **46**, 9, 1455-1460 (2011).
- Su Y.J., Pan K.L., Chang M.-B., *Modifying Perovskite-Type Oxide Catalyst $LaNiO_3$ with Ce for Carbon Dioxide Reforming of Methane*, *Int. J. Hydrogen Energy*, Vol. **39**, 4917-4925 (2014).
- Tudorache F. *et al.*, *Influence of Thermal Treatment on the Structure, Humidity Sensitivity, Electrical and Magnetic Properties of Barium-Tungsten Ferrite*, *Compos. Part B*, Vol. **51**, 106-111 (2013).
- Viviani M. *et al.*, *Barium Perovskites as Humidity Sensing Materials*, *J. Eur. Ceram. Soc.*, Vol. **21**, 1981-1984 (2001).
- Watanabe R., Saito Y., Fukuhara C., *Enhancement of Ethylbenzene Dehydrogenation of Perovskite-Type $BaZrO_3$ Catalyst by a Small Amount of Fe Substitution in the B-Site*, *J. Mol. Catal. A: Chem.*, Vol. **404**, 57-64 (2015).
- Xian H. *et al.*, *Effect of the Calcination Conditions on the NO_x Storage Behavior of the Perovskite $BaFeO_{3-x}$ Catalysts*, *Catal. Today*, Vol. **158**, 215-219 (2010).
- Zeng H.C., *Ostwald Ripening: A Synthetic Approach for Hollow Nanomaterials*, *Curr. Nanosci.*, Vol. **3**, 177-181 (2007).
- Zhang Y., Nan Z., *Modified Magnetic Properties of $MnFe_2O_4$ by CTAB with Coprecipitation Method*, *Mater. Lett.*, Vol. **149**, 22-24 (2015).
- Zhong G.Q., Xiong H., Jia Y.Q., *Synthesis, Crystal Structure, Relative Content of the Mn^{4+} Ion, Tolerance Factor and Catalytic Property of $La_{1-x}Ca_xMnO_3$ ($x=0.0-1.0$)*, *Mater. Chem. Phys.*, Vol. **91**, 10-16 (2005).

* ICDD $FeMnO_3$ -ICDD 75-0894, Fe_2O_3 – ICDD 89-2810.

INFLUENȚA AGENȚILOR DE COMBUSTIE ȘI A
TRATAMENTELOR TERMICE ASUPRA
PROPRIETĂȚILOR OXIZILOR FERICI DE MANGAN

(Rezumat)

Nanoparticule de oxizi ferici de mangan cu structură spinelică au fost sintetizate prin metoda sol-gel utilizând diferiți agenți de combustie și supuse ulterior unei serii de tratamente termice. Eșantioanele au fost caracterizate din punct de vedere structural, magnetic și electric. Măsurătorile magnetice au fost realizate la temperatura camerei prin intermediul unui sistem magnetometric cu probă vibrantă. Analizele de difractometrie au indicat că conținutul de fază după combustie și în diferite etape ale tratamentului termic este influențat de agentul de combustie folosit în procesul de sinteză. Dimensiunea cristalitelor eșantioanelor obținute este în domeniul nanometric. Măsurătorile magnetizației de saturație specifică și a câmpurilor coercitive au confirmat identificarea conținutului de fază. Măsurătorile permitivității și rezistivității electrice realizate pe eșantioanele conținând hexametilentetramină, uree și acid citric recomandă utilizarea acestora ca materiale de bază în confecționarea senzorilor.

BULETINUL INSTITUTULUI POLITEHNIC DIN IAȘI
Publicat de
Universitatea Tehnică „Gheorghe Asachi” din Iași
Volumul 62 (66), Numărul 3, 2016
Secția
MATEMATICĂ. MECANICĂ TEORETICĂ. FIZICĂ

THE ACCELERATION HORIZON AND THE THERMODYNAMICS OF ISOLATED PARTICLE

BY

ION SIMACIU*, ZOLTAN BORSOS, ANCA BACIU and GEORGETA NAN

Petroleum-Gas University of Ploiești,
Department of Informatics, Information Technology, Mathematics and Physics (ITIMF)

Received: October 27, 2016

Accepted for publication: December 10, 2016

Abstract. In this paper, we demonstrate the de Broglie's hypothesis of the existence of a thermodynamic particle is correct. For stochastic model of electron, we demonstrate that the electron as stochastic oscillator (system in accelerated motion) “sees” the stochastic Classical Zero-Point Field (CZPF) as a Planckian field with temperature equal to the anticipated de Broglie temperature ($T_o \cong mc^2/k_B$). Using the event horizon for a small bubble in vacuum that oscillating frequency equal to zitterbewegung frequency, we show that it behaves like an electric charge that have a stochastic motion and scattering the stochastic Classical Zero-Point Field (CZPF).

Keywords: Broglie's hypothesis; event horizon; Classical Zero-Point Field.

1. Introduction

The article is trying to establish a link between the isolated particle thermodynamics and the acceleration horizon in the framework of stochastic physics.

Louis de Broglie, in order to explain quantum effects as an interaction of microscopic systems with a sub-quantum environment, proposed a

*Corresponding author; *e-mail*: isimaciu@yahoo.com

thermodynamics of the isolated particle, *i.e.* the hidden thermodynamics of isolated particles (de Broglie, 1961; de Broglie, 1967) in which the particle is modelled as a thermodynamic system in interaction with the sub-quantum medium (the stochastic medium).

In the stochastic electrodynamics (stochastic physics of the charged particles), stochastic environment is modelled as a homogeneous and isotropic background of electromagnetic waves having randomly distributed phases.

Because this background is analogue the of the zero fluctuations background of the vacuum in quantum electrodynamics, was named Classical Zero-Point Field-CZPF (Puthoff, 1989; Boyer, 1969; Rueda, 1978; Rueda and Lecompte, 1979; Rueda, 1981; Rueda and Cavalleri, 1983).

To an accelerated observer (non-inertial) the electromagnetic radiation background with the zero temperature is perceived as a background of thermal radiation with temperature proportional to acceleration. This phenomenon is known as Unruh-Davies effect (Unruh, 1976; Davies, 1975). Timothy M. Boyer deduced the formula expressing the thermal radiation temperature depending on acceleration in the framework of the stochastic electrodynamics (Boyer, 1980).

In the second part of the paper we determine the average temperature corresponding to the modelled particles as an oscillator electrically charged in interaction with CZPF.

In the third part, we demonstrate that the angular frequency corresponding to the maximum (per Wien's displacement law) the Planckian background attached of the particle is angular frequency own of particle (modelled as a stochastic oscillator).

In the fourth part, we analyse the properties of the acceleration (Rindler, 2001) for a system (a particle) in oscillatory motion. We obtain the expressions of energy densities and the radiation entropy from the particle horizon. With these get to the expressions of energy, entropy and power corresponding to the particle horizon.

In the fifth part, we study the problem of the stochastic model horizon of electron and we find results like those of the second part.

The sixth part is devoted to discussions and conclusions.

2. The Average Temperature Corresponding to a Particle in Interaction with CZPF

A particle with the electric charge q_e and mass m is modelled like an oscillator with the natural angular frequency ω_0 in interaction with the CZPF background of vectors (Simaciu *et al.*, 1995; Simaciu and Ciubotariu, 2001).

$$\vec{E}_0(\vec{r}, t) = \text{Re} \sum_{\lambda=1}^2 \int d^3k \hat{e} \left(\frac{\hbar\omega}{8\pi^3 \epsilon_0} \right)^{1/2} \exp[-i(\omega t - \vec{k}\vec{r} - \theta)], \quad (1a)$$

$$\vec{H}_0(\vec{r}, t) = \text{Re} \sum_{\lambda=1}^2 \int d^3k (\hat{k} \times \hat{\epsilon}) \left(\frac{\hbar \omega}{8\pi^3 \mu_0} \right)^{1/2} \exp[-i(\omega t - \vec{k}\vec{r} - \theta)]. \quad (1b)$$

Below the action of CZPF (fund) background, the particle running a nonrelativistic oscillatory motion given by the equation

$$\ddot{\vec{r}} + \omega_0^2 \vec{r} = \frac{q}{m} \vec{E}_0 + \Gamma \ddot{\vec{r}}, \quad (2)$$

with the radiation damping coefficient $\Gamma = q^2/6\pi\epsilon_0 mc^3 = 2e^2/3mc^3$.

The solution of this equation is

$$\vec{r} = \frac{q}{Dm} \vec{E}_0, \quad (3)$$

with $D = \omega_0^2 - \omega^2 - i\Gamma\omega^3$ and $DD^* = |D|^2 = (\omega_0^2 - \omega^2)^2 + \Gamma^2\omega^6$.

The acceleration of the oscillator is

$$\vec{a} = \ddot{\vec{r}} = \frac{q}{Dm} \ddot{\vec{E}}_0 = \frac{q\omega^2}{Dm} \vec{E}_0. \quad (4a)$$

The average acceleration (we average after the random phase) is zero and the average square of the acceleration is

$$\langle \vec{a}^2 \rangle = \frac{q^2}{m^2} \left\langle \frac{\omega^4 \vec{E}_0^2}{|D|^2} \right\rangle \neq 0. \quad (4b)$$

Substituting the expression of the electric intensity of CZPF background (1a) in $\left\langle \omega^4 \left(\vec{E}_0^2 / |D|^2 \right) \right\rangle$ result that

$$\begin{aligned} \left\langle \frac{\omega^4 \vec{E}_0^2}{|D|^2} \right\rangle &= \frac{1}{2} \left\langle \text{Re} \sum_{\lambda=1}^2 \sum_{\lambda'=1}^2 \int \frac{\omega^4}{D^*} d^3k \int \frac{d^3k'}{D'} \hat{\epsilon} \hat{\epsilon}' \left(\frac{\hbar \omega}{8\pi^3 \epsilon_0} \right)^{1/2} \left(\frac{\hbar \omega'}{8\pi^3 \epsilon_0} \right)^{1/2} \right. \\ &\quad \left. \exp[i(\vec{k} - \vec{k}')\vec{r} - i(\omega - \omega')t + i\theta - i\theta'] \right\rangle = \\ &= \frac{1}{\epsilon_0} \int \frac{\hbar \omega^7}{2\pi^2 c^3 |D|^2} d\omega = \frac{1}{\epsilon_0} \int \frac{\omega^4 \rho(\omega)}{|D|^2} d\omega. \end{aligned} \quad (5)$$

If we replace in (5) the section of scattering of the plan-polarized radiation by the particle

$$\sigma(\omega) = \frac{\sigma_T \omega^4}{DD^*} = \frac{8\pi}{3} \left(\frac{e^2}{mc^2} \right)^2 \frac{\omega^4}{|D|^2} = \frac{6\pi \Gamma^2 c^2 \omega^4}{|D|^2}, \quad (6)$$

result that

$$\left\langle \frac{\omega^4 \bar{E}_0^2}{|D|^2} \right\rangle = \frac{3}{8\pi\epsilon_0} \left(\frac{mc^2}{e^2} \right)^2 \int \frac{\omega^4 \rho(\omega)}{|D|^2} d\omega. \quad (7)$$

Substituting (7) in (4) we obtain as follow

$$\begin{aligned} \langle \bar{a}^2 \rangle &= \frac{q^2}{m^2} \left\langle \frac{\omega^4 \bar{E}_0^2}{|D|^2} \right\rangle = \frac{3q^2}{8\pi\epsilon_0} \left(\frac{c^2}{e^2} \right)^2 \int \frac{\omega^4 \rho(\omega)}{|D|^2} d\omega = \\ &= \frac{3}{2} \left(\frac{c^4}{e^2} \right) \int \sigma(\omega) \rho(\omega) d\omega. \end{aligned} \quad (8)$$

Excepting a factor of the unity order that depends of the expression the scattering section of an isotropic background, according to the paper (Simaciu and Ciubotariu, 2001) integral

$$P_a = P_e = P_i = \int c\sigma(\omega)\rho(\omega)d\omega, \quad (9)$$

represent scattered power (the power absorbed is equal to the radiated power and therefore the CZPF background is scattered by oscillator) by the oscillator from CZPF.

Replacing (9) in (8) result the Larmor relationship (Jackson, 1975)

$$P_e = \frac{2}{3} \left(\frac{e^2}{c^3} \right) \langle \bar{a}^2 \rangle. \quad (10)$$

If is calculated the absorbed power according to the equation (9), result

$$P_a = \int_0^\infty c\sigma(\omega)\rho(\omega)d\omega = \frac{e^2 \hbar \omega_0^3}{mc^3}, \quad (11)$$

Equalling the two relations we obtain expression of the mean square acceleration

$$\langle \bar{a}^2 \rangle = \frac{3\hbar\omega_0^3}{2m} \quad (12)$$

and the average acceleration of the oscillator is

$$a_m = \sqrt{\langle \bar{a}^2 \rangle} = \omega_0 \sqrt{\frac{3\hbar\omega_0}{2m}}. \quad (13)$$

According to the works (Boyer, 1984), for particle accelerated the CZPF background becomes a Planckian background with temperature

$$T = \frac{\hbar}{2\pi ck_B} a \quad (14)$$

which also includes of the zero-point field.

Replacing (13) in (14) result:

$$T_o = \frac{\hbar}{2\pi ck_B} a_m = \frac{\hbar\omega_0}{k_B} \sqrt{\frac{3\hbar\omega_0}{8\pi^2 mc^2}}. \quad (15)$$

If the total energy of the oscillator (as a two-dimensional system with two degrees of freedom) is

$$mc^2 = \hbar\omega_0, \quad (16)$$

replacing (15) result:

$$T_o = \frac{\hbar}{2\pi ck_B} a_m \cong \frac{\hbar\omega_0}{k_B} \sqrt{\frac{3}{8\pi^2}} = \frac{mc^2}{k_B} \sqrt{\frac{3}{8\pi^2}}, \quad (17)$$

i.e. the oscillator acts as a particle submerged in a thermostat having the temperature proportional to the mass of the oscillator (de Broglie, 1961; de Broglie, 1962).

A similar result is obtained according to the approach made by Feynman (Feynman, 1964, Ch. 41, § 2) of an oscillator charged in interaction with the of equilibrium thermal radiation having the temperature T .

According to the relation (41.4) from (Feynman, 1964), the power radiated by an oscillator is proportional to the energy of the oscillator W_o

$$P_e = \Gamma W_o = \frac{2}{3} \left(\frac{e^2 \omega_0^2}{mc^3} \right) W_o. \quad (18)$$

If the oscillator is in equilibrium with a thermostat having the temperature T , its average (medium) energy is

$$W_o = 2 \frac{k_B T}{2} = k_B T, \quad (19)$$

for a one-dimensional oscillator.

Replacing (19) in (18) result

$$P_e = \Gamma W_o = \frac{2}{3} \left(\frac{e^2 \omega_0^2}{mc^3} \right) k_B T. \quad (20)$$

If the oscillator is in interaction with CZPF background, absorbed power is given by (11). Equalling (18) with (11) result the zero energy of the oscillator

$$W_o = 3 \frac{\hbar\omega_0}{2}. \quad (21)$$

Since the power absorbed was calculated for a three-dimensional oscillator, result that the energy for a one-dimensional oscillator in interaction with CZPF is

$$W_{o1} = \frac{\hbar\omega_0}{2}. \quad (22)$$

3. The Wien's Displacement Law for the Thermostat Attached of the Particle

According to Wien's displacement law (Boyer, 1984), the Planckian background attached of the particle has a maximum for the wavelength

$$\lambda_m T_d = \frac{ch}{x_m k_B}, x_m = 4,965 \quad (23a)$$

or

$$\lambda_m = \frac{ch}{x_m k_B T_d} \text{ or } \nu_m = \frac{c}{\lambda_m} = \frac{x_m k_B}{2\pi\hbar} T_o \text{ or } \omega_m = \frac{x_m k_B}{\hbar} T_o . \quad (23b)$$

Replacing the expression of the oscillator temperature (17) in (23b), result the remarkable relationship

$$\omega_m = \frac{mc^2}{\hbar} \sqrt{\frac{3x_m^2}{8\pi^2}} = \omega_0 \sqrt{\frac{3x_m^2}{8\pi^2}} \equiv \omega_0 . \quad (24)$$

Relation (24) demonstrates that the particle, as oscillator, absorbs and emits resonant from CZPF background, the natural angular frequency being angular frequency for which Planckian background has the spectral density $\rho(\omega, T)$.

4. The Properties of the Acceleration Horizon

4.1. The Horizon of a System in Accelerated Movement

A system in accelerated motion on Ox the direction, with acceleration a , perceive a horizon at distance (Rindler, 2001),

$$d_o = \frac{c^2}{a} . \quad (25)$$

The horizon is a plane perpendicular to the direction of movement located at distance given by (25)

From physical point of view, the existence of horizon is interpreted as limit until which the system can interact through fields that propagate at the speed of light. Systems located beyond the horizon, $x > d_o$, no longer interact with the system located in the origin of coordinates - are not causally related to accelerated system. In this case, area and volume of the horizon are infinite because on directions in the sense of the acceleration, horizon radius is infinite.

4.2. The Horizon of a System in Oscillatory Motion

Either a physical system which accomplish an oscillatory movement by amplitude q_0 and the angular frequency ω

$$q(t) = q_0 \sin(\omega t) . \quad (26)$$

Acceleration of this system is

$$\ddot{q} = q_0 \omega^2 \sin(\omega t) = \omega^2 q . \quad (27)$$

We consider that a particle in the physical vacuum is a bubble (Leighton, 1994). The radius of this bubble is at equilibrium R . The bubble

executes under the action of the vacuum waves radial oscillations of instant amplitude $q \ll R$, given by (26).

An observer at instantly rest on the surface of the bubble perceives a horizon of the acceleration by spherical form with variable radius.

Replacing equation (27) in the expression of the horizon distance result

$$r_o(t) = \frac{c^2}{\omega^2 q(t)} = \frac{c^2}{\omega^2 q_0 \sin(\omega t)} \quad (28)$$

and $c^2/\omega^2 q_0 \leq r_o(t) \leq \infty$.

The horizon radius relative to the centre of the bubble is

$$R_o(t) = R + r_o(t) = R + \frac{c^2}{\omega^2 q(t)}. \quad (29)$$

This radius of the horizon mediated in time can be calculated using the average acceleration of the horizon surface

$$a_m = \sqrt{\langle (\ddot{q})^2 \rangle_t} = q_0 \omega^2 \sqrt{\langle \sin^2(\omega t) \rangle_t} = \frac{q_0 \omega^2}{\sqrt{2}}. \quad (30)$$

With this average acceleration, average radius of horizon as against the bubble centre is

$$R_m = R + \frac{c^2 \sqrt{2}}{\omega^2 q_0}. \quad (31)$$

The average area of horizon is

$$A_m = 4\pi R_m^2 = 4\pi R^2 \left(1 + \frac{\sqrt{2} c^2}{R q_0 \omega^2} \right)^2 \quad (32)$$

and

$$V_m = \frac{4\pi}{3} R_m^3 = \frac{4\pi}{3} R^3 \left(1 + \frac{\sqrt{2} c^2}{R q_0 \omega^2} \right)^3 \quad (33)$$

is the volume of the accelerate horizon.

4.3. Energy's and Entropy's Densities from Particle Horizon

The observer from bubble surface perceives the CZPF background of a of background of thermal radiation having temperature proportional to acceleration, according to the relation (14).

The energy density of this radiation is

$$w = \frac{4\sigma_{SB}}{c} T^4. \quad (34)$$

Replacing (14) in (34) result

$$w(a) = \frac{\sigma_{SB} \hbar^4}{2^2 \pi^4 c^5 k^4} a^4. \quad (35)$$

Because the Stefan-Boltzmann constant has the expression

$$\sigma_{SB} = \frac{3(1,082)k^4}{2\pi^2 c^2 \hbar^3}, \quad (36)$$

resulting, through replacement within (35)

$$w(a) = \frac{3(1,082)\hbar}{2^3 \pi^6 c^7} a^4. \quad (37)$$

The expression of entropy density of the radiation is

$$w_s(a) = \int \frac{dw(a)}{T(a)} = \frac{2^4 \sigma_{SB}}{3c} (T(a))^3. \quad (38)$$

Replacing (14) and (36) in (38), result

$$w_s(a) = \frac{(1,082)k}{\pi^5 c^6} a^3. \quad (39)$$

4.4. Energy, Entropy and Power of Particle Horizon

The energy contained by the horizon with radius given by the relations (31) and having the volume given by (33) is, with $a = a_m$

$$W(a_m) = V_m w(a_m) = \frac{(1,082)\hbar}{2\pi^5 c} \left(1 + \frac{Rq_0\omega^2}{c^2\sqrt{2}}\right)^3 \frac{q_0\omega^2}{\sqrt{2}}. \quad (40)$$

The entropy contained in the horizon volume is with (33) and (38), for $a = a_m$

$$S(a_m) = V_m w_s(a_m) = \frac{4(1,082)}{3\pi^4} \left(1 + \frac{Rq_0\omega^2}{c^2\sqrt{2}}\right)^3 k. \quad (41)$$

We find corresponding power for this radiation considering that is emitted through the area the horizon (32), with $a = a_m$

$$P(a_m) = A_m I(a_m) = A_m \frac{cw(a_m)}{3} = \frac{(1,082)\hbar}{2\pi^5 c^2} \left(1 + \frac{Rq_0\omega^2}{c^2\sqrt{2}}\right)^2 \left(\frac{q_0\omega^2}{\sqrt{2}}\right)^2. \quad (42)$$

If we consider approximation of small oscillations, that is $q_0 \ll R$, $c/\omega \gg q_0$ and $Rq_0\omega^2/c^2 \ll 1$, result that entropy from volume of the horizon is a constant

$$S(a_m) \cong \frac{4(1,082)}{3\pi^4} k \quad (43)$$

and dispersed power (absorbed and emitted, at equilibrium) is of Larmor type

$$P(a_m) \cong \frac{(1,082)\hbar}{2\pi^5 c^2} \left(\frac{q_0 \omega^2}{\sqrt{2}} \right)^2 = \frac{(1,082)\hbar}{2\pi^5 c^2} a_m^2, \quad (44)$$

i.e. it is power emitted of an accelerated electric charge. According to the classical theory, a charged particle with electrical charge and which is in an accelerated motion radiates a power given by Larmor relation (Jackson, 1975)

$$P_L = \frac{2}{3} \frac{e^2}{c^3} a^2 = \frac{2}{3} \left(\frac{e^2}{\hbar c} \right) \frac{\hbar}{c^2} a^2. \quad (45)$$

Comparing relations (45) and (46), result, with $a = a_m$

$$\frac{e^2}{\hbar c} = \frac{3(1,082)}{2^2 \pi^5}. \quad (46)$$

The difference between the two values is relatively small: $e^2/\hbar c \cong 1/137$ and $3(1,082)/(2^2 \pi^5) \cong 1/102$. Improving the model can lead to parameter values which determine the equality of constants.

5. The Horizon of Stochastic Model for Electron

In stochastic physics (Simaciu and Ciubotariu, 2001) the electron is a two-dimensional oscillator (circular motion), that changes the plan of the circular motion with zitter frequency (equivalent of movement on a sphere). Result that this model is just a case of generating a spherical acceleration horizon.

According to this model, the speed on orbit is $v = c$, and replacing in (25) and (29) with $R = R_e$ result the centripetal acceleration and the horizon radius:

$$a_{ce} = \frac{c^2}{R_e}, \quad (47)$$

$$R_{oce} = 2 \frac{c^2}{a_{ce}} = 2R_e. \quad (48)$$

Replacing those sizes in the energy expressions (40) and power (42), with $a = a_m = a_{ce}$ result

$$W_e(a_{ce}) = V(a_{ce})w(a_{ce}) = \frac{2^2(1,082)\hbar}{\pi^5 c} a_{ce}, \quad (49)$$

$$P_e(a_{ce}) = \frac{(1,082)\hbar}{\pi^5 c^2} a_{ce}^2. \quad (50)$$

Outside of the acceleration horizon, is issued radiation with power given by relations (50 and 51). According to the classical theory of the oscillator

electrically charged, this radiates a power given by relation (45) which becomes, with $a = a_{ce}$,

$$P_L = \frac{2}{3} \left(\frac{e^2}{\hbar c} \right) \frac{\hbar}{c^2} \cdot a_{ce}^2. \quad (51)$$

Comparing the expression (51) with expressions of power emitted by the accelerating horizon (51) or (50), result that power issued of the horizon could be interpreted as the power radiated by oscillator, if the coefficients front the expression $\hbar a_{ce} / c^2$ are equal. These coefficients have the values:

$$\frac{2}{3} \left(\frac{e^2}{\hbar c} \right) = 4,86 \cdot 10^{-3}, \quad \frac{1,082}{\pi^5} = 3,53 \cdot 10^{-3}. \quad (52)$$

The coincidence of expressions powers is not accidental. We found the result from Section 4.4. An analysis more exact for mechanisms for the generating of horizon for a system which execute a moving of oscillation three-dimensional, is likely to lead to better coincidence of the powers relations.

If we replace in the expression (49) the acceleration corresponding to the model of electron, $R_e = \hbar / m_e c$, $a_{ce} = m_e c^3 / \hbar$ result:

$$W_e(a_{ce}) = \frac{2^2 (1,082) \hbar}{\pi^5 c} \cdot \frac{m_e c^3}{\hbar} = \frac{2^2 (1,082)}{\pi^5} m_e c^2.$$

It follows that there is a connection between the thermal radiation energy captured in the volume of horizon and energy electron $m_e c^2$.

6. Discussion and Conclusions

We emphasized the fact that de Broglie's hypothesis about the existence a thermodynamic of the particle is correct. In the case of electron stochastic model, we demonstrated that the electron as stochastic oscillator and therefore system in accelerated motion "sees" the CZPF background like a Planckian background with temperature equal to the anticipated one by Broglie ($T_o \cong mc^2/k_B$).

It is interesting that the angular frequency corresponding to the maximum of spectral density of the Planckian background is equal to the natural frequency of the stochastic oscillator (expression 24). This behaviour of the stochastic oscillator is consistent with bubble model (a hole in the physical vacuum) oscillating radially, for an electrically charged particle. The oscillations are induced and maintained by the interaction of the bubble with the zero oscillations of the vacuum. At equilibrium bubble absorbs and emits waves with angular frequency nearly, as size, to the natural frequency. For electron, this is the zitterbewegung frequency. According the results section 4 and 5, the two models, punctual task that absorbs and emits radiation of CZPF (in other

words scattered this radiation) and the bubble in vacuum radial's oscillating (centre bubble's is at rest) are equivalent.

Two such bubbles interact with forces of attraction or repulsion, depending on the phase difference of the oscillations. This phenomenon is known in acoustic as Bjerknes secondary interaction (Bjerknes, 1906; Bjerknes, 1915; Bărbat *et al.*, 1999). This interaction has been studied theoretically and experimentally only in case the two bubbles are in the field of plane acoustic waves that propagate or is stationary. The highlighting a task acoustic electric type is made only studying the interaction two bubbles with a thermal background of acoustic waves. In this case the bubble absorbs energy from the background, at resonance, for natural frequency. This acoustic model will be studied in a future study.

The existence of a spherical horizon, for the particle models proposed in the paper, brings into question and the existence of gravitational charge corresponding to the particle. This connection exists because the gravitational interaction for a body with mass involves a horizon of events in case collapsing at a radius equal to the Schwarzschild radius (the radius of black hole) (Rindler, 2001).

REFERENCES

- Bărbat T., Ashgriz N., Liu C.S., *Dynamics of Two Interacting Bubbles in an Acoustic Field*, J. Fluid Mech., **389**, 137-168 (1999).
- Bjerknes C.A., *Hydrodynamische Fernkraft*, Engelmann, Leipzig (1915).
- Bjerknes V.F.K., *Fields of Force*, Columbia University Press, New York (1906).
- Boyer T., *Classical Statistical Thermodynamics and Electromagnetic Zero - Point Radiation*, Phys. Rev., **186**, 1304 (1969).
- Boyer T., *Thermal Effects of Acceleration Through Random Classical Radiation*, Phys. Rev. **D21**, p. 2137 (1980).
- Boyer T., *Thermal Effects of Acceleration for Classical Dipole Oscillator in Classical Electromagnetic Zero - Point Radiation*, Phys. Rev. **D29**, 1089 (1984); **D30**, 1228 (1984).
- Davies P.C.W., *Scalar Particle Production in Schwarzschild and Rindler Metrics*, J. Phys. **A8**, p. 609-616 (1975).
- de Broglie L., *La Thermodynamique de la particule isolée*, C.R. Acad. Sc., 253, p. 1078 (1961); 255, p. 807 and p. 1052 (1962).
- de Broglie L., *La mouvement brownian d'une particule dans son onde*, C. R. Acad. Sc. Paris, **264**, SB, 1041 (1967).
- Feynman R.P., Leighton R.B., Matthew S., *The Feynman Lectures on Physics*, Volume **1**, Addison-Wesley, Reading (1964).
- Jackson J. D., *Classical Electrodynamics*, 2nd Ed., Wiley, New York (1975).
- Leighton T.G., *The Acoustic Bubble*, London, Academic Press (1994).
- Puthoff H. E., *Sources of Vacuum Electromagnetic Zero - Point Energy*, Phys. Rev. **A40**, 4857 (1989)
- Rindler W., *Relativity: Special, General and Cosmological*, Oxford: Oxford University Press (2001).

- Rueda A., *Model of Einstein and Hopf for Protons in Zero - Point Field and Cosmic - Ray Spectrum*, Nuovo Cimento, **48A**, 155 (1978).
- Rueda A., *Behavior of Classical Particles Immersed in the Classical Electromagnetic Zero-Point Field*, Phys. Rev. **A23**, 4, 2020-2040 (1981).
- Rueda A., Lecompte A., *On Approximations in the Model of Einstein and Hopf*, Nuovo Cimento, **52A**, 264-275 (1979).
- Rueda A., Cavalleri G., *Zitterbewegung in Stochastic Electrodynamics and Implication on a Zero - Point Field Acceleration Mechanism*, Nuovo Cimento, **6C**, 239 (1983).
- Simaciu I., Ciubotariu C., *Classical Model of Electron in Stochastic Electrodynamics*, Revista Mexicană de Fizică, **47**, 4, 392-394 (2001).
- Simaciu I., Dumitrescu Gh., Dinu M., *New Results in Stochastic Physics*, Romanian Reports in Physics, **47**, 6/7, 537-556 (1995).
- Unruh W.G., *Notes on Black-Hole Evaporation*, Phys. Rev. **D14**, 870-892 (1976).

ORIZZONTUL ACCELERĂRII ȘI TERMODINAMICA PARTICULEI IZOLATE

(Rezumat)

În lucrare demonstrăm că ipoteza lui de Broglie a existenței unei termodinamici a particulei este corectă. În cazul modelului stocastic de electron demonstrăm că electronul, ca oscilator stocastic și deci sistem în mișcare accelerată, “vede” fondul CZPF ca un fond planckian cu temperatura egală cu cea anticipată de Broglie ($T_o \cong mc^2/k_B$). Folosind orizontul evenimentelor, pentru o bulă din vacuum care execută mici oscilații egale cu frecvența de zitterbewegung, arătăm că aceasta se comportă ca o sarcină electrică care se mișcă stocastic și împrăștie Classical Zero-Point Field (CZPF).

BULETINUL INSTITUTULUI POLITEHNIC DIN IAȘI
Publicat de
Universitatea Tehnică „Gheorghe Asachi” din Iași
Volumul 62 (66), Numărul 3, 2016
Secția
MATEMATICĂ. MECANICĂ TEORETICĂ. FIZICĂ

NON-DIFFERENTIABLE PROCESSES

BY

IRINEL CASIAN BOTEZ*

“Gheorghe Asachi” Technical University of Iași,
Faculty of Electronics, Telecommunication and Information Technology

Received: November 18, 2016

Accepted for publication: December 19, 2016

Abstract. Our purpose in this paper is to underline the limitations of ordinary differential equations of motion for providing dynamical basis for complex phenomena which justify our approach of using scale relativity theory.

Keywords: Non-differentiable processes; scale relativity theory.

1. Linear Physics

In 1695 Leibniz speculate on the idea of calculating a derivative of order 0.5, in response to a request from L'Hospital. However, in physics, such things as fractional derivatives, have been left aside in favour of long study analytic functions. It was supposed, probably since Galileo, that the physical phenomena can be largely represented by analytic functions and dynamics of physical phenomena can be represented mathematically by equations of motion in which such functions are involved. The truth of this assumption was almost confirmed by Sturm-Liouville Theory success in formalizing acoustic or electromagnetic phenomena, transmission of heat, diffusion or quantum processes. Even when phenomena like phase transitions, turbulence and rheology of polymeric materials could not be explained using the approach

*Corresponding author; *e-mail*: irinel_casian@yahoo.com

mentioned above, it is believed that the solution can come from a more detailed analysis of the same type.

2. Nonlinear Physics

In the last 45 years, working methodologies in physics have changed, abandoning more and more the linear mathematical methods, analytical and quantitative (Stoyan, 1979; Benoit, 1982; West and Deering, 1994; Schroeder, 2009; Meakin, 2011), heading for a combination of nonlinear mathematical methods, numerical and quantitative (Meakin, 2011). Not only linear methods often have proved inadequate, but even the Euclidean geometry use has not always proved adequate. In any case, Newton formulated the mechanical laws using geometric arguments, although he had developed earlier the differential calculus. Nowhere in “Principia” you will find the famous equation, $\mathbf{F} = m\mathbf{a}$, nor any discussion about derivatives or solving differential equations, but you will find used geometry of Euclid and reports of geometric lengths which are presumed to converge on finite values when the size of timeframes tends to zero. Default felled everywhere in “Principia” is the notion of limit, but nowhere is explicitly discussed this concept. Newton's dynamic arguments are based on the assumption of an absolute space and absolute time, the dimensions are without beginning or end and the continuity is everywhere. The allegations of a continuous and infinite time and space, combined with Euclidean geometry, almost guarantees the continuity of measurements of derived quantities as speed, acceleration and force.

3. Questioning of Differentiability

In the context of modern physics, we learned that the assumptions of absolute space and time are no longer valid and the Euclid's geometry has little to do with physical world. In his lessons about the principles of mechanics, Ludwig Boltzmann (1974), the father of statistical physics, said “... *we have, without apology, presented differentiability as an assumption that agrees with the experimental facts to date*”.

But this assumption was invalidated in many cases, of which we evoke here three: a) the problem of turbulence: in 1926, Richardson (Richardson, 1926) published his research on irregular fluctuations in the velocity field of turbulent wind in the atmosphere; b) Levy Statistics: Levy (Levy, 1925; Bologna *et al.*, 2002) has set the most general properties needed by a statistical process to violate accepted form, at that time, of the central limit theorem but yet to converge to a limit distribution; c) Brownian motion: the dynamic of this process, developed by Langevin in 1908 using a stochastic differential equation (Levy, 1954) is incompatible with continuous and differentiable nature of the

microscopic Hamiltonian dynamics. The differentiability of empirical functions of mechanics is something given by the observational tools which are at our disposal and so nothing precludes, in fact, the use of non-differentiable functions to represent the experimental results. There are at least as many differentiable functions as those non-differentiable. An example of such functions are fractal functions for which an illustrious example being generalized Weierstrass function:

$$F(t) = \sum_{n=-\infty}^{+\infty} \frac{1}{a^n} \sin[b^n t + \phi_n] \quad (1)$$

which has the derivative:

$$\frac{dF(t)}{dt} = \sum_{n=-\infty}^{+\infty} \left(\frac{b}{a}\right)^n \cos[b^n t + \phi_n] \quad (2)$$

If $b > a$, the series (2) diverge in an absolute manner when $n \rightarrow \infty$. Note that the function (1) may be either a deterministic fractal function (if the phases $\{\phi_n\}$ are zero), or a stochastic fractal function (in the phases $\{\phi_n\}$ are random).

4. Central Limit Theorem (CLT)

There is a link between the non-differentiability of microscopic processes (Abbott and Wise, 1981), the differentiability of macroscopic processes and the CLT conditions. Let we remind that, according to central limit theorem, if $w_1(t)$, $w_2(t)$, ..., are statistically independent stochastic processes, with identically distribution, than the sum variable:

$$w(t) = \sum_{n=1}^{\infty} w_n(t) \quad (3)$$

is a Gaussian stochastic process.

CLT applies to dynamical systems that have the time scale of microscopic processes much smaller than the time scale for macroscopic processes. In this situation of separation between the two time scales, on long duration, the memory of details given by microscopic dynamics is lost and we can apply a Gaussian statistics on the result at the macroscale. This separation of time scales also means that we can use again ordinary differential calculus at macroscopic scale, even if microscopic dynamics is incompatible with ordinary differential calculus.

5. Two Time Scales

Whether the two time scales are different or not, we must resort to statistical physics. There are two approaches enshrined in this physics. One is the approach of Heisenberg that use dynamic variables. In this approach, in the case of the separation between the two time scales, the transition from microscopic to macroscopic leads to a stochastic differential equation of Langevin type for a macroscopic dynamic variable which corresponds to a random process with Gaussian distribution. The second approach uses Schrodinger's perspective according to which the time evolution of a Liouville density defined in the phase space of the system. The result of this approach is a master equation that usually leads to a conventional diffusion equation, which is a partial differential equation, of second order in relation to space and first-order in relation to time. Therefore, in case of separation of time scales between microscopic and macroscopic, the mathematical description remains in the field of conventional differentiable analytic functions which describe the dynamics (Heisenberg's approach, centred on particle) or the conventional differential operator (second order partial derivatives in Schrodinger's approach, centred on the wave). These two approaches were considered equivalent thought for a hundred years, until this equivalence was questionable when different solutions, to the same physical problem, have been obtained using these two approaches (Bologna *et al.*, 2002).

When the separation between microscopic time scale and macroscopic time scale is not valid, the memory of non-differentiable nature of the phenomena at the microscopic level is preserved. Thus, transport equations cannot be expressed in terms of ordinary differential calculus, even if our observation is macroscopically.

6. Conclusions

Inability of using macroscopically the ordinary differential calculus is the explanation why the temporal derivative in Langevin equation is replaced by a fractional derivative in relation with time, obtaining a fractional stochastic equation. Likewise, Laplace operator of normal diffusion equation is replaced by a fractional Laplace operator, yielding a fractional diffusion equation in the phase space of the system. We have developed these arguments in (Agop and Casian-Botez, 2015; Agop *et al.* 2015; Casian-Botez and Agop, 2015a; Casian-Botez and Agop, 2015b; Casian-Botez *et al.*, 2015).

REFERENCES

- Abbott L.F., Wise M.B., *Dimension of a Quantum - Mechanical Path*, American Journal of Physics, **49**, 1, 37-39 (1981).
- Agop M., Casian-Botez I., *Theoretical Approach of Differentiable-Non-Differentiable Scale Transition in Nanostructures*, Journal of Computational and Theoretical Nanoscience, **12**, 9, 2140-2151 (2015).
- Agop M., Casian-Botez I. *et al.*, *On the Memorizing Ability of Nanostructures*, Journal of Computational and Theoretical Nanoscience, **12**, 4, 682-688 (2015).
- Benoit M.B., *The Fractal Geometry of Nature*, W.H. Freeman and Company (1982).
- Bologna M., Grigolini P. *et al.*, *Strange Kinetics: Conflict Between Density and Trajectory Description*, Chemical Physics, **284**, 1-2, 115-128 (2002).
- Boltzmann L., *Lectures on the Principles of Mechanics*, Theoretical Physics and Philosophical Problems: Selected Writings. B. McGuinness. Dordrecht, Springer Netherlands, 223-254 (1974).
- Casian-Botez I., Agop M., *Coherence-Type Behaviours in Nanostructures*, Journal of Computational and Theoretical Nanoscience, **12**, 2, 263-269 (2015a).
- Casian-Botez I., Agop M., *Order Disorder Transition in Nanostructures via Non-Differentiability*, Journal of Computational and Theoretical Nanoscience, **12**, 8, 1746-1755 (2015b).
- Casian-Botez I., Vrăjitoriu L. *et al.*, *Interferential Behaviors in Nanostructures via Non-Differentiability*, Journal of Computational and Theoretical Nanoscience, **12**, 8, 1483-1489 (2015).
- Levy P., *Calcul Des Probabilites*, Paris, Gauthier-Villars (1925).
- Levy P., *Theorie De L'Addition Des Variables Aleatoires*, Paris, Gauthier-Villars, (1954).
- Meakin P., *Fractals, Scaling and Growth Far from Equilibrium*, Cambridge University Press; Reissue Edition (2011).
- Richardson L.F., *Atmospheric Diffusion Shown on a Distance-Neighbour Graph*, Proceedings of the Royal Society of London A: Mathematical, Physical and Engineering Sciences, **110**, 756, 709-737 (1926).
- Schroeder M., *Fractals, Chaos, Power Laws*, Dover Publications, Inc. (2009).
- Stoyan D. , *Mandelbrot, B. B., Fractals: Form, Chance, and Dimension*. San Francisco, W.H. Freeman and Company, 1977, 352 S., 68 Abb., \$14.95, ZAMM - Journal of Applied Mathematics and Mechanics/Zeitschrift für Angewandte Mathematik und Mechanik, **59**, 8, 402-403 (1979).
- West B.J., Deering W., *Fractal Physiology for Physicists: Lévy Statistics*, Physics Reports, **246**, 1, 1-100 (1994).

PROCESE NEDIFERENȚIABILE

(Rezumat)

Scopul nostru în această lucrare este de a sublinia limitările ecuațiilor diferențiale ordinare de mișcare pentru a pune bazele descrierii dinamici fenomenelor complexe prin utilizarea teoriei relativității de scară.